Geosci. Model Dev. Discuss., 7, 4705–4775, 2014
www.geosci-model-dev-discuss.net/7/4705/2014/
doi:10.5194/gmdd-7-4705-2014

Geoscientific Model Development Discussions
Open Access

Mass-conserving subglacial hydrology in the Parallel Ice Sheet Model

E. Bueler[1] **and W. Van Pelt**[2,*]

[1]Department of Mathematics and Statistics, University of Alaska Fairbanks, Alaska, USA
[2]Institute for Marine and Atmospheric Research Utrecht, the Netherlands
[*]now at: Norwegian Polar Institute, Tromsø, Norway

Received: 20 June 2014 – Accepted: 10 July 2014 – Published: 29 July 2014

Correspondence to: E. Bueler (elbueler@alaska.edu)

Published by Copernicus Publications on behalf of the European Geosciences Union.

Abstract

We describe and test a distributed subglacial hydrology model which combines a pressurized, plastic till with a system of water-filled, linked cavities which open through sliding-generated cavitation and close through ice creep. The addition of this sub-model to the Parallel Ice Sheet Model accomplishes three specific goals: (1) conservation of the mass of two-phase (solid/liquid) water in the ice sheet, (2) simulation of spatially- and temporally-variable basal shear stress from physical mechanisms based on a minimal number of free parameters, and (3) convergence under two-horizontal-dimensional grid refinement of the subglacial water amount and pressure. The model is a common generalization of at least four others: (i) the undrained plastic bed model of Tulaczyk et al. (2000b), (ii) a standard "routing" model used for identifying locations of subglacial lakes, (iii) the lumped englacial/subglacial model of Bartholomaus et al. (2011), and (iv) the elliptic-pressure-equation model of Schoof et al. (2012). We use englacial porosity as a regularization, and we preserve physical bounds on the pressure. In steady state the model generates a local functional relationship between water amount and pressure. We construct an exact solution of the coupled, steady equations which is used for verification of our explicit time-stepping, parallel numerical implementation. We demonstrate the model at scale by five year simulations of the entire Greenland ice sheet at 2 km horizontal resolution, with one million nodes in the hydrology grid.

1 Introduction

Any reasonable dynamical model of the liquid water underneath and within a glacier or ice sheet has at least these two elements: the mass of the water is conserved and the water flows from high to low values of the modeled hydraulic potential. Beyond that there are many variations considered in the literature. Modeled aquifer geometry might be a system of linked cavities (Kamb, 1987), conduits (Nye, 1976), or a sheet (Creyts and Schoof, 2009). Geometry evolution processes might include the opening of

GMDD
7, 4705–4775, 2014

cavities by sliding of the overlying ice past bedrock bumps (Schoof, 2005), the creation of cavities by interaction of the ice with deformable sediment (Schoof, 2007), closure of cavities and conduits by creep (Hewitt, 2011), or melt on the walls of cavities and conduits which causes them to open (Clarke, 2005). Water could move in a macroporous englacial system (Bartholomaus et al., 2011; Harper et al., 2010) or it could be stored in a porous till (Tulaczyk et al., 2000a).

Successful models have combined subsets of these different morphologies and processes – for examples see Flowers and Clarke (2002a), Hewitt (2013), van der Wel et al. (2013), Werder et al. (2013), and de Fleurian et al. (2014). It is not, however, always true that adding more processes makes a better model. Especially when used to understand variations in ice flow and sliding, which is a goal here, the completeness of the modeled processes should be balanced against the number of uncertain model parameters and the ultimate availability of observations with which to constrain them.

This paper describes a carefully-selected model for a distributed system of linked subglacial cavities, with additional storage of water in the pore spaces of subglacial till. The mass conservation equation in our model describes the evolution of the sum of the transportable water in the distributed system and the water stored in the till. Water in excess of the capacity of the till passes into the transport system, and in this sense the model could be called a "drained-and-conserved plastic bed" extension of the "undrained plastic bed" model of Tulaczyk et al. (2000b).

The goals of the current work are the implementation, verification, and practical demonstration of this two-dimensional subglacial hydrology model. It must also be parallelizable, apply at a wide variety of spatial and temporal scales, exhibit convergence of solutions under grid refinement, and have as few parameters as practical. The result is a sub-model of a comprehensive three-dimensional ice sheet model, the open-source Parallel Ice Sheet Model (PISM; pism-docs.org). The submodel can be added to any PISM run by a simple run-time option.

The cavities in our modeled distributed system open by sliding of the ice over bedrock roughness and they close by ice creep, two physical processes which combine to

GMDD
7, 4705–4775, 2014

determine the relationship between water amount and pressure. Pressure is thereby determined non-locally over each connected component of the hydrological system. No functional relation between subglacial water amount and pressure is assumed (compare Flowers and Clarke, 2002a). The subglacial water pressure solves an equation which is a parabolic regularization of the distributed pressure equation given in elliptic variational inequality form by Schoof et al. (2012).

In cases where boreholes have actually been drilled to the ice base, till is observed (Hooke et al., 1997; Tulaczyk et al., 2000a; Truffer et al., 2000; Truffer and Harrison, 2006). Laboratory experiments on the rheology of till (Kamb, 1991; Hooke et al., 1997; Tulaczyk et al., 2000a; Truffer et al., 2001) generally conclude that its deformation is well-approximated by a Mohr–Coulomb relation (Schoof, 2006b). For this reason we adopt a compressible-Coulomb-plastic till model when determining the effective pressure on the till as a function of the amount of water stored in it (Tulaczyk et al., 2000a). Existing models which combine till and a mass conservation equation for the subglacial water are rather different from ours, as they either have only one-horizontal dimension (van der Wel et al., 2013) or have a pressure equation which directly ties water pressure to water amount, which generates a porous medium equation form (Flowers and Clarke, 2002a; de Fleurian et al., 2014).

Wall melt in the linked-cavity system can be calculated diagnostically from the modeled flux and hydraulic gradient. If included as a contribution to the mass conservation equation, however, the addition of wall melt generates an unstable distributed system (Walder, 1982), though such a system can be stabilized to some degree by bedrock bumps (Creyts and Schoof, 2009). In this model, wall melt is not added into the mass conservation equation.

Conduits are also not included in our model. While the pressure and amount of water in conduits could evolve by physical processes, the existing theory of conduits apparently requires their locations to be fixed a priori (Schoof, 2010b; Pimentel and Flowers, 2011; Hewitt et al., 2012; Hewitt, 2013; Werder et al., 2013). Such lattice models have no known continuum limit in the map plane. Because all PISM usage

GMDD
7, 4705–4775, 2014

involves a run-time determination of grid resolution, which varies from 40 km to 10 mm in the applications documented in the PISM User's Manual (PISM authors, 2013), all parameters must have grid-spacing-independent meaning. Lattice or other fixed-grid models are therefore not acceptable as components of PISM.

The structure of the paper is as follows: Sect. 2 considers basic physical principles, culminating with a fundamental advection-diffusion form of the mass conservation equation. Section 3 reviews what is known about till mechanical properties, water in till pore spaces, and shear stress at the base of a glacier. In Sect. 4 we compare closures which directly or indirectly determine the subglacial water pressure. Based on all these elements, in Sect. 5 we summarize the new model and the role of its major fields. In this section we also show how the model extends several published models, and we note properties of its steady states; see also Appendix A. In Sect. 6 we compute an exact steady solution in the map-plane, a useful tool for verification. In Sect. 7 we present all numerical schemes, with particular attention to time step restrictions and the treatment of advection. Section 8 documents the PISM options and parameters seen by a user. Section 9 shows numerical results from the model, including convergence under grid refinement in the verification case, and a demonstration of the model in five year runs on a 2 km grid covering the entire Greenland ice sheet.

2 Elements of subglacial hydrology

2.1 Mass conservation

We assume that liquid water is of constant density. Thus the thickness of the layer of laterally-transportable (mobile) water, denoted by $W(t,x,y)$, determines its mass. In addition there is liquid water stored locally in the pore spaces of till (Tulaczyk et al., 2000b) which is also described by an effective thickness $W_{\text{till}}(t,x,y)$. Such thicknesses are only meaningful compared to observations if they are regarded as averages over a horizontal scale of tens to thousands of meters (Flowers and Clarke, 2002a).

GMDD
7, 4705–4775, 2014

The total effective thickness of the water at map-plane location (x, y) and time t is $W + W_{\text{til}}$. This sum is the conserved quantity in our model. In two map-plane dimensions the mass conservation equation is (compare Clarke, 2005)

$$\frac{\partial W}{\partial t} + \frac{\partial W_{\text{til}}}{\partial t} + \nabla \cdot \boldsymbol{q} = \frac{m}{\rho_{\text{w}}} \tag{1}$$

where $\nabla \cdot = (\partial/\partial x) + (\partial/\partial y)$ denotes divergence, $\boldsymbol{q}$ is the (vector) water flux (units $\text{m}^2\,\text{s}^{-1}$), m is the total input to the subglacial hydrology (units $\text{kg}\,\text{m}^{-2}\,\text{s}^{-1}$) and ρ_{w} is the density of fresh liquid water; see Table 1 for this and other physical constants. Note that the water flux $\boldsymbol{q}$ is concentrated within the two-dimensional subglacial layer.

The water source m in Eq. (1) includes melt on the lower surface of the glacier and drainage from the glacier upper surface if that occurs. In portions of ice sheets with cold surface conditions, such as Antarctica and the interior of Greenland, the basal melt rate part of m is primarily determined by the energy balance at the base of the ice (Aschwanden et al., 2012). The Greenland results in Sect. 9 use only that basal melt for m. Drainage from the surface has also been added to m in applications of our model (van Pelt, 2013), but modelling such drainage is outside the scope of this paper.

2.2 Hydraulic potential

The hydraulic potential $\psi(t, x, y)$ combines the pressure $P(t, x, y)$ of the transportable subglacial water and the gravitational potential of the top of the water layer (Goeller et al., 2013; Hewitt et al., 2012),

$$\psi = P + \rho_{\text{w}} g\,(b + W). \tag{2}$$

Here $z = b(x, y)$ is the bedrock elevation.

We have added the term "$\rho_{\text{w}} g W$" to the standard hydraulic potential formula $\psi = P + \rho_{\text{w}} g b$ (Clarke, 2005; Shreve, 1972) because differences in the potential at the *top* of the subglacial water layer determine the driving potential gradient for a fluid layer. The

GMDD
7, 4705–4775, 2014

W term in Eq. (2) makes the mass conservation equation diffusive, regardless of the action of other diffusive mechanisms; see Sect. 5.3. When the water depth becomes substantial ($W \gg 1$ m), as it would be in a subglacial lake, this term keeps the modeled lakes from being singularities of the water thickness field. Indeed, subglacial lakes of infinitesimal extent and infinite depth form at local minima of the hydraulic potential if this term is absent (Le Brocq et al., 2009).

Ice is a viscous fluid which has a stress field of its own. The basal value of the downward normal stress, traditionally called the overburden pressure, is denoted by P_o. We accept the shallow approximation that it is hydrostatic (Greve and Blatter, 2009):

$$P_o = \rho_i g H, \tag{3}$$

where H is the ice thickness. Because the condition $P > P_o$ is presumed to cause the ice to lift and thus reduce the pressure back to overburden $P = P_o$ (Schoof et al., 2012), it follows that the pressure solution is subject to inequalities

$$0 \le P \le P_o. \tag{4}$$

In temperate glaciers a similar upper bound applies because water rising to the surface through efficient englacial conduits is free to flow at the surface, ensuring $P \le (\rho_w/\rho_i)P_o$, at least if supraglacial geysers are regarded as exceptional (Bartholomaus et al., 2011).

2.3 Darcy flow

Transportable water flows from high to low hydraulic potential. The simplest expression of this is a Darcy flux model for a water sheet,

$$\boldsymbol{q} = -K W \nabla \psi \tag{5}$$

where the hydraulic conductivity K is a constant (Clarke, 2005). More generally Schoof et al. (2012) suggests

$$\boldsymbol{q} = -k W^{\alpha} |\nabla \psi|^{\beta-2} \nabla \psi \tag{6}$$

GMDD
7, 4705–4775, 2014

for $\alpha \geq 1$, $\beta > 1$, and a coefficient $k > 0$ with units that depend on α and β (see Table 1). The power-law form Eq. (6) is justified as an instance of a Manning or Darcy–Weisbach law (Schoof et al., 2012). Clarke (2005) suggests $\alpha = 1$ and $\beta = 2$, to give Eq. (5) above, Creyts and Schoof (2009) use $\alpha = 3/2$ and $\beta = 3/2$, Hewitt (2011, 2013) uses $\alpha = 3$ and $\beta = 2$, and Hewitt et al. (2012) suggest $\alpha = 5/4$ and $\beta = 3/2$. The current paper implements law Eq. (6) generally but uses the Clarke (2005) and Hewitt et al. (2012) exponents in an exact solution and in numerical experiments, respectively. When we use Eq. (6) we call $K = k W^{\alpha-1} |\nabla\psi|^{\beta-2}$ the *effective* hydraulic conductivity, so that Eq. (5) applies formally throughout.

2.4 Advection-diffusion decomposition

Combining Eqs. (2) and (6), and separating the term proportional to ∇W, we get the flux expression

$$\boldsymbol{q} = -kW^{\alpha} |\nabla\psi|^{\beta-2} \nabla (P + \rho_{\mathrm{w}} g b) - \rho_{\mathrm{w}} g k W^{\alpha} |\nabla\psi|^{\beta-2} \nabla W. \tag{7}$$

The second term with ∇W acts diffusively in the mass conservation Eq. (1). On the other hand, because P generally scales with the overburden pressure P_{o}, the first flux term in Eq. (7) will dominate in the common situation $|\nabla H| \gg |\nabla W|$. We will see in Sect. 5.3 that in near-steady-state circumstances the part of the transport velocity which is proportional to ∇P is also significantly diffusive in the mass conservation equation. In conditions far from steady state, however, the direction of ∇P is different from the direction ∇W.

We will construct our conservative numerical scheme based on decomposition Eq. (7). To simplify the model slightly, the small thickness approximation $W \approx 0$ is made inside the absolute value signs in Eq. (7), namely

$$|\nabla\psi| \approx |\nabla (P + \rho_{\mathrm{w}} g b)|. \tag{8}$$

GMDD
7, 4705–4775, 2014

This simplification, which makes no change in the $\beta = 2$ case, lets us redefine the effective hydraulic conductivity as

$$K = kW^{\alpha-1}|\nabla(P + \rho_w g b)|^{\beta-2}. \tag{9}$$

In terms of K we define a velocity field and a diffusivity coefficient:

$$\boldsymbol{V} = -K\,\nabla(P + \rho_w g b), \qquad D = \rho_w g K W. \tag{10}$$

Now Eq. (7) is a clean advection-diffusion decomposition,

$$\boldsymbol{q} = \boldsymbol{V}W - D\nabla W. \tag{11}$$

From Eqs. (1) and (11) we now have an advection-diffusion-production equation for the evolution of the water amount:

$$\frac{\partial W}{\partial t} + \frac{\partial W_{\text{til}}}{\partial t} = -\nabla\cdot(\boldsymbol{V}W) + \nabla\cdot(D\nabla W) + \frac{m}{\rho_w}. \tag{12}$$

There are distinct numerical approximations (Sect. 7) for the advection term $\nabla\cdot(\boldsymbol{V}W)$ and the diffusion term $\nabla\cdot(D\nabla W)$, and they impose time-step restrictions of different magnitudes. We will see that Eq. (12) is often advection-dominated in the sense that $|\boldsymbol{V}W| \gg |D\nabla W|$, but the numerical schemes for advection and diffusion must be tested in combination. We measure convergence of the combined numerical schemes in Sect. 9.

As is well known (Clarke, 2005), the flux $\boldsymbol{q}$ depends significantly on the ice surface slope because the ice overburden pressure dominates the subglacial water pressure. The model in this paper also generates pressure fields with this property in some circumstances, but the directions of hydraulic potential gradient and surface gradient are significantly different in general because the pressure depends on physical mechanisms for the opening and closing of cavities.

GMDD
7, 4705–4775, 2014

2.5 Capacity of a linked-cavity distributed system

The rate of change of the area-averaged thickness of the cavities in a distributed linked-cavity system can be described as the difference of opening and closing rates (Hewitt, 2011). This thickness Y, also called the bed separation (Bartholomaus et al., 2011), has evolution equation

$$\frac{\partial Y}{\partial t} = \mathcal{O}(|\boldsymbol{v}_b|, Y) - \mathcal{C}(N, Y) \tag{13}$$

where $\boldsymbol{v}_b$ is the ice base (sliding) velocity and $N = P_o - P$ is the effective pressure on the cavity system. Denoting $X_+ = \max\{0, X\}$, we choose an opening term based on cavitation only:

$$\mathcal{O}(|\boldsymbol{v}_b|, Y) = c_1 |\boldsymbol{v}_b| (W_r - Y)_+. \tag{14}$$

Here W_r is a maximum roughness scale of the basal topography (Schoof et al., 2012). The closing term models ice creep only (Hewitt, 2011; Schoof et al., 2012):

$$\mathcal{C}(N, Y) = c_2 A N^3 Y. \tag{15}$$

We have used Glen exponent $n = 3$ for concreteness and simplicity. By Eq. (14) the opening term $\mathcal{O}$ is nonnegative, and the closing term $\mathcal{C}$ in Eq. (15) is also nonnegative because our modeled pressure P satisfies bounds $0 \le P \le P_o$.

The physical intuition behind a model which combines Eq. (13) with mass conservation Eq. (1) and a Darcy flux relation like Eq. (6) is as follows. If the cavity is larger than local water sources can immediately fill then the pressure should drop. Lower pressure encourages water inflow and, by Eq. (15), it speeds cavity closure, bringing the pressure back up. Conversely, if local water sources exceed capacity then increased pressure should push water out of the area and slow creep closure.

GMDD
7, 4705–4775, 2014

3 Till hydrology and mechanics

In areas where the ice base is not frozen, till with pressurized liquid water in its pore spaces can be expected to support much of the ice overburden. When present, such saturated till is central to the complicated relationship between the amount of subglacial water and the speed of sliding. Our model includes storage of subglacial water in till, potentially everywhere under the ice sheet, both because of its role in conserving the mass of liquid water and its role in determining basal shear stress.

We will assume throughout that liquid water or ice fills pore spaces in the till, and that there are no air- or vapor-filled pore spaces. We suppose that when $W_{\text{til}} = 0$ then the pore spaces in the till are filled with ice and the basal shear stress is correspondingly-high. When W_{til} is small the till will generally hold both liquid water and ice. Only when W_{til} attains sufficiently large values is the till conceived-of as entirely melted, at which point a drop in effective pressure becomes possible (Sect. 3.2 below).

3.1 Evolution of water amount

While the thickness W in Eq. (1) describes the amount of mobile water in subglacial cavities, and in the connections between cavities (Kamb, 1987), the water in till pore spaces is much less mobile because of the very low hydraulic conductivity of till (Lingle and Brown, 1987; Tulaczyk et al., 2000a; Truffer et al., 2001). Therefore we choose an evolution equation for W_{til} for simplicity (Bueler and Brown, 2009), namely

$$\frac{\partial W_{\text{til}}}{\partial t} = \frac{m}{\rho_{\text{w}}} - C_{\text{d}}. \tag{16}$$

Here $C_{\text{d}} \geq 0$ is a fixed rate that makes the till gradually drain in the absence of water input. Equation (16) is the same as Eq. (2) in Tulaczyk et al. (2000b). In practice we choose $C_{\text{d}} = 1\,\text{mm}\,\text{a}^{-1}$, which is small compared to typical values of m/ρ_{w}. Refreeze is also allowed, as a negative value for m. Note that any water removed from the till enters the transport system; it is conserved.

GMDD
7, 4705–4775, 2014

3.2 Effective pressure on the till

There is extensive evidence that deformation of saturated till is well-modeled by a plastic (Coulomb friction) or nearly-plastic rheology (Hooke et al., 1997; Truffer et al., 2000; Tulaczyk et al., 2000a; Schoof, 2006b). The yield stress τ_c of such till satisfies the Mohr–Coulomb relation

$$\tau_c = c_0 + (\tan\varphi) N_{til} \tag{17}$$

where c_0 is the till cohesion, φ is the till friction angle, and N_{til} is the effective pressure of the overlying ice on the saturated till (Cuffey and Paterson, 2010). (The effective pressure $N = P_o - P$ used in the next section for modeling cavity closure is distinct from N_{til} in Eq. (17). This distinction is justified by the very low hydraulic conductivity of till.)

Let $e = V_w/V_s$ be the till void ratio, where V_w is the volume of water in the pore spaces and V_s is the volume of mineral solids (Tulaczyk et al., 2000a). From the standard theory of soil mechanics and from laboratory experiments on till (Hooke et al., 1997; Tulaczyk et al., 2000a), a linear relation exists between the logarithm of N_{til} and e,

$$e = e_0 - C_c \log_{10}\left(N_{til}/N_0\right). \tag{18}$$

Figure 1a shows a graph of Eq. (18). Here e_0 is the void ratio at a reference effective pressure N_0 and C_c is the coefficient of compressibility of the till. Equivalently, N_{til} is an exponential function of e, namely $N_{til} = N_0 10^{(e_0-e)/C_c}$ (van der Wel et al., 2013, Eq. 15). Note that in Eq. (18), N_{til} is nonzero for all finite values of e.

While Eq. (18) suggest that the effective pressure could be any positive number, in fact the area-averaged value of N_{til} under ice sheets and glaciers has limits. It cannot exceed the overburden pressure for any sustained period. Furthermore, once the till is close to its maximum capacity then the excess water will be "drained" into a transport system. We suppose this occurs at a small, fixed fraction of the overburden pressure. Thus we assume bounds

$$\delta P_o \le N_{til} \le P_o \tag{19}$$

GMDD
7, 4705–4775, 2014

where $\delta = 0.02$ in the experiments in this paper.

The void ratio e and the effective water layer thickness W_{til} are describing the same thing, namely the amount of liquid water. In fact, if Δx, Δy are the horizontal dimensions of a rectangular patch of till then $V_{\text{w}} = W_{\text{til}}\,\Delta x\,\Delta y$ and $V_{\text{s}} = \eta\,\Delta x\,\Delta y$ where η is the thickness of the mineral portion of the till. Because $e = V_{\text{w}}/V_{\text{s}}$ it follows that

$$e = \frac{W_{\text{til}}}{\eta}. \tag{20}$$

On the other hand we will describe the maximum capacity of the till by specifying a maximum on the water layer thickness (Bueler and Brown, 2009), that is,

$$0 \le W_{\text{til}} \le W_{\text{til}}^{\max}. \tag{21}$$

The minimum $N_{\text{til}} = \delta P_{\text{o}}$ of the effective pressure occurs at the maximum void ratio e and at maximum W_{til}. But then Eqs. (18) and (20) combine to express the solid-till thickness η in terms of our preferred parameters and the overburden pressure,

$$\eta = \frac{W_{\text{til}}^{\max}}{e_0 - C_{\text{c}} \log_{10}\left(\delta P_{\text{o}}/N_0\right)}. \tag{22}$$

From Eqs. (18), (20), and (22), the effective pressure N_{til} can now be written as the following function of W_{til}:

$$\hat{N}_{\text{til}} = N_0 \left(\frac{\delta P_{\text{o}}}{N_0}\right)^{s} 10^{(e_0/C_{\text{c}})(1-s)} \tag{23}$$

where $s = W_{\text{til}}/W_{\text{til}}^{\max}$. However, as noted above, N_{til} is bounded, so the form we use is shown in Fig. 1b:

$$N_{\text{til}} = \min\left\{P_{\text{o}}, \hat{N}_{\text{til}}\right\}. \tag{24}$$

It follows from Eqs. (17) and (24) that the yield stress τ_{c} can be determined from the water amount W_{til}. Regarding the parameters in this relation:

GMDD
7, 4705–4775, 2014

i. Experiments on till suggest small values for cohesion, $0 \le c_0 \lesssim 1\,\mathrm{kPa}$ (Tulaczyk et al., 2000a), and we choose $c_0 = 0$ for concreteness.

ii. Observed till friction angles φ are in a $18^\circ - 40^\circ$ range (Cuffey and Paterson, 2010). Simulations of the whole Antarctic (Martin et al., 2011) and Greenlandic (Aschwanden et al., 2013) ice sheets have been based on a hypothesis that the till friction angle φ can depend on bed elevation, so as to accommodate the submarine history of some sediments.

iii. The ratio e_0/C_c can be determined by laboratory experiments on till samples (e.g. Hooke et al., 1997; Tulaczyk et al., 2000a). Values for the dimensionless constants e_0 and C_c used in this paper are from till samples from ice stream B in Antarctica, namely $e_0 = 0.69$ and $C_c = 0.12$ in Fig. 6 of Tulaczyk et al. (2000a), thus $e_0/C_c = 5.75$.

iv. The till capacity parameter W_{til}^{max} could be set in a location-dependent manner from in situ (Tulaczyk et al., 2000a) or seismic reflection (Rooney et al., 1987) evidence, but for simplicity we set it to a constant 2 m.

3.3 Sliding law

The ice sliding velocity is determined by solving a stress balance in which the vector basal shear stress $\boldsymbol{\tau}_b$ appears either as a boundary condition (Schoof, 2010a) or as a term in the balance (Schoof, 2006a; Bueler and Brown, 2009). In PISM the scalar yield stress τ_c determines the basal shear stress through a sliding law

$$\boldsymbol{\tau}_b = -\tau_c \frac{\boldsymbol{u}}{|\boldsymbol{u}|^{1-q} u_0^q} \tag{25}$$

where $\boldsymbol{u}$ is the sliding velocity of the base of the ice, $0 \le q \le 1$, and u_0 is a threshold sliding velocity (Aschwanden et al., 2013). Power law (Eq. 25) generalizes, and includes as the case $q = 0$, the purely-plastic (Coulomb) relation $\boldsymbol{\tau}_b = -\tau_c \boldsymbol{u}/|\boldsymbol{u}|$. At least in the

GMDD
7, 4705–4775, 2014

$q \ll 1$ cases, under Eq. (25) the till "yields" and the magnitude of the basal shear stress becomes nearly independent of $|\boldsymbol{u}|$ as $|\boldsymbol{u}| \gg u_0$. Equation (25) could also be written in generic power-law form $\boldsymbol{\tau}_b = -\beta|\boldsymbol{u}|^{q-1}\boldsymbol{u}$ with coefficient $\beta = \tau_c/u_0^q$; in the linear case $q = 1$ we have $\beta = \tau_c/u_0$.

4 Closures to determine pressure

The evolution equations listed so far, namely Eqs. (12), (13), and (16), can be simplified to three equations in the four major variables W, W_{til}, Y, and P. We do not yet know how to compute the water pressure P or its rate of change $\partial P/\partial t$ given the other variables and data of the problem. A closure is needed.

4.1 Simplified closures without cavity evolution

We first consider two simple closures which appear in the literature but which do not use cavity evolution Eq. (13) or similar physics. These simplified closures differ in their physical motivation and the form of their mass conservation equations. We list them because the resulting simplified conservation equations emerge as reductions of our more complete theory. For simplicity we present them without till storage, that is, with $W_{til}^{max} = 0$ in previous equations. We state only the constant conductivity case ($\alpha = 1$ and $\beta = 2$ in Eq. 6).

Setting the pressure equal to the overburden pressure is the simplest closure (Le Brocq et al., 2009; Shreve, 1972):

$$P = P_o. \tag{26}$$

This model is sometimes used for "routing" subglacial water under ice sheets so as to identify subglacial lake locations (Livingstone et al., 2013; Siegert et al., 2009). Straightforward calculations using Eqs. (1), (5), and (26) show that the

GMDD
7, 4705–4775, 2014

advection-diffusion form Eq. (12) has an ice-geometry-determined velocity,

$$\frac{\partial W}{\partial t} = -\nabla\cdot\left(\tilde{\boldsymbol{V}}\,W\right) + \nabla\cdot(\rho_{\mathrm{w}} g K\, W\, \nabla W) + \frac{m}{\rho_{\mathrm{w}}} \tag{27}$$

where

$$\tilde{\boldsymbol{V}} = -\rho_{\mathrm{w}} g K \left[\frac{\rho_{\mathrm{i}}}{\rho_{\mathrm{w}}}\nabla h + \left(1 - \frac{\rho_{\mathrm{i}}}{\rho_{\mathrm{w}}}\right)\nabla b\right]. \tag{28}$$

Because the approximation $W \ll H$ is usually accepted, so that the hydraulic potential is insensitive to the water layer thickness, i.e. $\psi = P_{\mathrm{o}} + \rho_{\mathrm{w}} g b$ (Le Brocq et al., 2009), the diffusion term $\nabla\cdot(\rho_{\mathrm{w}} g K\, W\, \nabla W)$ on the right of Eq. (27) is usually not included. With this common simplification, Eq. (27) becomes a pure advection with a velocity $\tilde{\boldsymbol{V}}$ which is independent of W. It therefore possesses characteristic curves (Evans, 1998) which are the *a priori* known trajectories of the water flow. These trajectories are determined by ice sheet geometry.

However, without a diffusion term (Eq. 27) also exhibits continuum solutions W with infinite water concentration at every location where the simplified potential $\psi = P_{\mathrm{o}} + \rho_{\mathrm{w}} g b$ has a minimum. Applications using the simplified potential only compute the characteristic curves (i.e. "pathways", Livingstone et al., 2013) themselves. We therefore prefer Eq. (27) as stated, *with* the diffusion term, because it is well-posed for positive initial and boundary values on W (compare Hewitt et al., 2012), so numerical solutions can converge under sufficient grid refinement.

At an almost opposite extreme in terms of the mathematical form, the second simplified closure we consider assumes that the water pressure is locally determined by the amount of water. Specifically, Flowers and Clarke (2002a) propose

$$P_{\mathrm{FC}}(W) = P_{\mathrm{o}}\left(\frac{W}{W_{\mathrm{crit}}}\right)^{7/2}. \tag{29}$$

GMDD
7, 4705–4775, 2014

For Trapridge glacier Flowers and Clarke (2002b) use $W_{\text{crit}} = 0.1$ m. Thus no separate pressure evolution equation needs to be solved (Pimentel et al., 2010; Pimentel and Flowers, 2011). One obvious concern with form Eq. (29) is that $P_{\text{FC}}(W)$ can be arbitrarily larger than overburden pressure (Schoof et al., 2012).

In the flat bedrock case $\nabla b = 0$, we can derive an equation from Eqs. (1), (5), and (29), namely

$$\frac{\partial W}{\partial t} = \nabla \cdot (k W \nabla P_{\text{FC}}(W)) + \frac{m}{\rho_{\text{w}}}. \tag{30}$$

Equation (30) is a nonlinear diffusion which generalizes the porous-medium equation $\partial W/\partial t = \nabla^2(W^\gamma)$ (Schoof et al., 2012; Vázquez, 2007). The main idea in such a nonlinear diffusion is that the direction of the flux is $-\nabla W$. Physically, however, it would seem that $\boldsymbol{q} \sim -\nabla\psi$ would give flux directions different from $-\nabla W$ in many cases, especially in rapidly-evolving hydrologic systems.

4.2 Full-cavity closure

Requiring the subglacial layer to be full of water is a closure for the subglacial pressure P. Following Bartholomaus et al. (2011), we adopt it in our model:

$$W = Y. \tag{31}$$

The consequences of this closure are actually explored at some length by Schoof et al. (2012), Hewitt et al. (2012), and Werder et al. (2013), where they describe the full-cavity case as the "normal pressure" condition (e.g. Eq. 4.13 in Schoof et al., 2012).

Equation (31) obviously allows us to eliminate either W or Y as a state variable. We choose to eliminate Y because W is part of the conserved mass $W + W_{\text{til}}$. Using Eqs. (1), (13), and (31) we can then derive

$$\mathcal{O}(|\boldsymbol{v}_{\text{b}}|, W) - C(N, W) + \frac{\partial W_{\text{til}}}{\partial t} + \nabla \cdot \boldsymbol{q} = \frac{m}{\rho_{\text{w}}}. \tag{32}$$

GMDD
7, 4705–4775, 2014

In the zero till storage case (set $W_{til}^{max} = 0$ so $W_{til} = 0$), Eq. (32) is exactly the elliptic pressure equation (Eq. 2.12) of Schoof et al. (2012). They solve Eq. (32) in one dimension with pressure boundary conditions at the lateral edges of the subglacial hydrologic system to determine the pressure P, and they argue that a model based on Eq. (32) should accommodate the possibility of partially-empty cavities with $W < Y$ and at zero pressure $P = 0$. Direct evidence for such vapor/air-filled cavities does not exist for tidewater glaciers or ice sheets, though of course subglacial hydrology is poorly-observed generally. In any case we accept a potential loss of model completeness by using a full-cavity model.

Overpressure $P > P_o$ has been observed in ice sheets (Das et al., 2008; Bartholomaus et al., 2011, for example), but only for short durations. Our modelled pressure satisfies $P \le P_o$; compare Werder et al. (2013).

4.3 Notional englacial porosity as a regularization

Englacial systems of cracks, crevasses, and moulins have been observed in glaciers (Fountain et al., 2005; Bartholomaus et al., 2008; Harper et al., 2010, for example), and these have been included in combined englacial/subglacial hydrology models (Flowers and Clarke, 2002a; Bartholomaus et al., 2011; Hewitt, 2013; Werder et al., 2013). The englacial system is generally parameterized as having macroporosity $0 \le \phi < 1$. If the englacial system is efficiently-connected to the subglacial hydrology then the amount of englacial water is equivalent to the subglacial pressure. Subglacial pressure is reflected by an englacial "water table" in such models.

Bueler (2014) shows that an extension of the lumped englacial/subglacial model in Bartholomaus et al. (2011) to the distributed case gives an equation similar to Eq. (32), but with the crucial difference that the equation is parabolic for the pressure and not elliptic (compare Hewitt et al., 2012). Based on this analysis, we use a parabolic equation

GMDD
7, 4705–4775, 2014

with constant notional englacial porosity $\phi = \phi_0$:

$$\frac{\phi_0}{\rho_w g}\frac{\partial P}{\partial t} = -\nabla\cdot\boldsymbol{q} + \frac{m}{\rho_w} + C(N,W) - \mathcal{O}(|\boldsymbol{v}_b|,W) - \frac{\partial W_{til}}{\partial t}. \quad (33)$$

Compare Eq. (7) in Hewitt (2013) and Eq. (24) in Werder et al. (2013).

Addition of englacial porosity as in Eq. (33) allows a user-adjustable trade-off between temporal detail in the pressure evolution vs. computational effort (van Pelt, 2013). If the englacial porosity ϕ_0 is small, so that there is a nearly impermeable "cap" on the subglacial system, as would occur under a thick ice sheet, then Eq. (33) is stiff (Ascher and Petzold, 1998) and indeed similar, in terms of numerical solution, to an elliptic equation. By contrast, if ϕ_0 is relatively large then Eq. (33) causes local changes in subglacial pressure P to be damped in the speed and range of their influence on other parts of the connected subglacial hydrologic system. In fact, the diffusive range of Eq. (33) is proportional to ϕ_0. If the elliptic Eq. (32) is used instead of Eq. (33) then the system in Sect. 5 (below) is differential-algebraic in time (Ascher and Petzold, 1998) and is hardest to solve numerically.

Schoof et al. (2012) show that the time-independent mathematical problem encompassing Eq. (32), constraints Eq. (4), and appropriate pressure boundary conditions can be written as an elliptic variational inequality (Kinderlehrer and Stampacchia, 1980). This variational inequality problem is asserted to be "prohibitively expensive" by Werder et al. (2013) when solved in two dimensions at each step of a time-stepping model. Our adaptive explicit time-stepping scheme (Sect. 7), by contrast, satisfies constraints Eq. (4) at demonstrably-reasonable computational cost (Sect. 9).

Stiffness of pressure equation (Eq. 33) follows from the incompressibility of water and the relative non-distensibility (i.e. hardness) of the ice and bedrock. Clarke (2003) addresses this in a physically-different way by including a relaxation (damping) parameter "β" which is based on the small compressibility of water, but which is more than two orders of magnitude larger than the physical value. Clarke's parameter β appears in his equation exactly as the englacial porosity ϕ_0 appears in Eq. (33), multiplying the pressure time derivative.

GMDD
7, 4705–4775, 2014

5 A new subglacial hydrology model in PISM

5.1 Summary of equations and symbols

The major evolution equations for the model are mass conservation (Eq. 12), till-stored water amount evolution (Eq. 16), and pressure evolution (Eq. 33). Recalled here for clarity they are:

$$\frac{\partial W}{\partial t} + \frac{\partial W_{\text{til}}}{\partial t} = -\nabla\cdot(\boldsymbol{V} W) + \nabla\cdot(D\nabla W) + \frac{m}{\rho_{\text{w}}}, \tag{34}$$

$$\frac{\partial W_{\text{til}}}{\partial t} = \frac{m}{\rho_{\text{w}}} - C_{\text{d}},$$

$$\frac{\phi_0}{\rho_{\text{w}} g}\frac{\partial P}{\partial t} + \frac{\partial W_{\text{til}}}{\partial t} = -\nabla\cdot(\boldsymbol{V} W) + \nabla\cdot(D\nabla W) + \frac{m}{\rho_{\text{w}}} + c_2 A (P_{\text{o}} - P)^3 W - c_1 |\boldsymbol{v}_{\text{b}}| (W_{\text{r}} - W)_+,$$

using these definitions:

$D = \rho_{\text{w}} g K W$	diffusivity of W
$K = k W^{\alpha-1} \lvert\nabla(P + \rho_{\text{w}} g b)\rvert^{\beta-2}$	effective conductivity
$P_{\text{o}} = \rho_{\text{i}} g H$	overburden pressure
$s = W_{\text{til}} / W_{\text{til}}^{\max}$	W_{til} relative to capacity
$\boldsymbol{V} = -K\nabla(P + \rho_{\text{w}} g b)$	velocity of W.

The model includes bounds on major variables: $0 \le W$, $0 \le W_{\text{til}} \le W_{\text{til}}^{\max}$, $0 \le P \le P_{\text{o}}$. The model is also coupled to ice dynamics by Mohr–Coulomb equation (Eq. 17) and till effective pressure equation (Eq. 24), namely

$$\tau_{\text{c}} = c_0 + (\tan\varphi) N_{\text{til}}, \tag{35}$$

$$N_{\text{til}} = \min\left\{P_{\text{o}}, N_0 \left(\frac{\delta P_{\text{o}}}{N_0}\right)^s 10^{(e_0/C_{\text{c}})(1-s)}\right\}.$$

GMDD
7, 4705–4775, 2014

The functions used above can be categorized into *state* functions, which must be provided with initial values and which evolve according to the model, *input* functions, which are either supplied by observations or by other components of an ice sheet model (e.g. the stress balance in an ice dynamics model will provide $|\boldsymbol{v}_b|$), and *output* functions which are supplied to other components of the ice sheet model (e.g. the yield stress τ_c is fed back to the stress balance); see Table 2. In two-way coupling the ice dynamics model passes H, m, and $|\boldsymbol{v}_b|$ to the subglacial hydrology model, and τ_c is passed the other way.

5.2 Reduction to existing models

Four reductions (limiting cases) of model Eq. (34) can now be stated precisely:

i. The zero till storage ($W_{til}^{max} = 0$) and zero englacial porosity ($\phi_0 = 0$) case of Eq. (34) is the model described by Schoof et al. (2012), recalling that $\boldsymbol{q} = -KW\nabla\psi$,

$$\frac{\partial W}{\partial t} = -\nabla\cdot(KW\nabla\psi) + \frac{m}{\rho_w}, \qquad (36)$$
$$0 = \nabla\cdot(KW\nabla\psi) + \frac{m}{\rho_w} + c_2 A(P_o - P)^3 W - c_1|\boldsymbol{v}_b|(W_r - W)_+.$$

The bounds $W \geq 0$ and $0 \leq P \leq P_o$ are unchanged. Model Eq. (34) is a parabolic regularization of Eq. (36) based on a notional connection to porous englacial storage, and with coupling to additional till storage.

ii. The $P = P_o$ limit of Eq. (34), in which physical processes for the evolution of pressure are ignored, is essentially the model for "routing" water to subglacial lakes under cold ice sheets in Siegert et al. (2009) and Livingstone et al. (2013). Assuming again that till storage is removed ($W_{til}^{max} = 0$) then the model has only W

GMDD
7, 4705–4775, 2014

as a state variable, the single evolution equation is

$$\frac{\partial W}{\partial t} = -\nabla\cdot(\boldsymbol{V}W) + \nabla\cdot(D\nabla W) + \frac{m}{\rho_{\mathrm{w}}}. \tag{37}$$

along with the bound $W \geq 0$ and further-simplified definitions $K = kW^{\alpha-1}|\nabla(P_{\mathrm{o}} + \rho_{\mathrm{w}}gb)|^{\beta-2}$ and $\boldsymbol{V} = -K\nabla(P_{\mathrm{o}} + \rho_{\mathrm{w}}gb)$. As noted in Sect. 4, the $\alpha = 1$ case of this model routes water with a velocity which is determined entirely by ice and bedrock geometry. This reduced model is mostly an advection, but, because of Eq. (2) for the hydraulic potential, which implies some diffusion, model Eq. (37) has continuous solutions for W.

iii. The non-distributed "lumped" form of Eq. (34), in which, in particular, $\nabla\cdot\boldsymbol{q} = (q_{\mathrm{out}} - q_{\mathrm{in}})/L$ where L is the length of a one-dimensional glacier and $q_{\mathrm{out}}, q_{\mathrm{in}}$ are given by observations, is the model of Bartholomaus et al. (2011); see Bueler (2014).

iv. The undrained plastic bed (UPB) model of Tulaczyk et al. (2000b) arises as the $W = 0, \boldsymbol{q} = 0, \phi_0 = 0$ reduction of Eq. (34). This lumped model depends on friction-heating feedback to keep W_{til} bounded, which is not effective in a membrane-stress-inclusive theory in which local friction heating is a non-local function of changes in till strength. Bueler and Brown (2009) therefore enforce $W_{\mathrm{til}} \leq W_{\mathrm{til}}^{\mathrm{max}}$ by non-conservatively removing water above the capacity, which is a minimal "drained" version of the UPB model.

The above list does not imply that all possible subglacial hydrology models are subsumed in ours. For example, the subglacial hydrology model of Johnson and Fastook (2002) is a variation on idea (ii) above but it is not a reduction. The Flowers and Clarke (2002a) model is also not a reduction, although a significant connection is explained in the section on steady states below. Most significantly, models which include conduits (Schoof, 2010b; Pimentel and Flowers, 2011; Hewitt et al., 2012, among others) are not reductions of our model. Conduit evolution is numerically-straightforward to implement in one-dimensional hydrology models (Pimentel and Flowers, 2011; Hewitt et al.,

GMDD
7, 4705–4775, 2014

2012; van der Wel et al., 2013) but when extended to two-horizontal dimensions all existing models (Schoof, 2010b; Hewitt, 2013; Werder et al., 2013) become "lattice" models without a known continuum limit.

5.3 Steady states

The steady states of Eq. (34) are of physical modelling importance because the subglacial system can be close to steady state much of the time, but also because physical processes become decoupled in steady state, and this helps us understand the model. Specifically, the steady form of model Eq. (34), with $\alpha = 1$, $\beta = 2$, and $W_{\text{til}}^{\max} = 0$ for simplicity, can be written as follows in terms of $\boldsymbol{V}, \boldsymbol{q}, W, P$:

$$\boldsymbol{V} = -k\nabla(P + \rho_{\text{w}} g b), \tag{38}$$

$$\boldsymbol{q} = \boldsymbol{V} W - \rho_{\text{w}} g k W \nabla W, \tag{39}$$

$$0 = -\nabla \cdot \boldsymbol{q} + \frac{m}{\rho_{\text{w}}}, \tag{40}$$

$$0 = c_2 A (P_{\text{o}} - P)^3 W - c_1 |\boldsymbol{v}_{\text{b}}| (W_{\text{r}} - W)_+. \tag{41}$$

Steady state Eqs. (38)–(41) are stated in the one-dimensional case by Schoof et al. (2012) model, where the decoupling is also noted; see Eqs. (5.8) and (5.10) in Schoof et al. (2012).

We can make four specific observations about solutions to Eqs. (38)–(41), which we find are useful in understanding the time-dependent model at longer time-scales also:

i. from Eq. (41) there is a functional relationship $P = P(W)$ which determines the pressure given the water amount,

ii. by Eqs. (38) and (41), the apparently advective flux "$\boldsymbol{V}W$" in Eq. (39) actually acts diffusively, if sliding is occurring and if the water amount is either small or comparable to the roughness scale,

GMDD
7, 4705–4775, 2014

iii. by Eqs. (39) and (40) the water amount W generally scales inversely with the conductivity, and

iv. exact solutions can be constructed.

In Appendix A we detail points (i), (ii), and (iii). Observation (iv) is addressed in the next section.

6 An exact steady state solution

6.1 Radial equations

Steady Eqs. (38)–(41) are the basis on which we now build a nearly-exact solution for W and P in the map-plane, in a case with nontrivial overburden pressure and ice sliding speed. This solution is useful for verifying numerical schemes. It depends on the numerical solution of a scalar first-order ordinary differential equation (ODE) initial value problem, something we can do with high accuracy. Traveling wave exact solutions in one horizontal dimension also appear in Schoof et al. (2012).

Consider the flat bed case ($b = 0$). Assuming dependence only on the radial coordinate $r = \sqrt{x^2 + y^2}$, from Eqs. (38)–(40) one may eliminate the velocity to get

$$q = -kW\left(\frac{\mathrm{d}P}{\mathrm{d}r} + \rho_w g \frac{\mathrm{d}W}{\mathrm{d}r}\right), \tag{42}$$

$$\frac{1}{r}\frac{\mathrm{d}}{\mathrm{d}r}(r\,q) = \frac{m}{\rho_w}. \tag{43}$$

In the case of constant water input $m = m_0$, we can integrate Eq. (43) from 0 to r and use symmetry ($q(0) = 0$) to get

$$q(r) = \frac{m_0}{2\rho_w} r. \tag{44}$$

GMDD
7, 4705–4775, 2014

Suppose $H(r)$ is given so that $P_o(r)$ is also determined. Assume that the scaled sliding speed $s_b(r)$ has a bounded derivative and that the solution $W(r)$ satisfies conditions $W_c < W < W_r$; these properties can be verified for the constructed solution. By combining Eqs. (A4), (A5), (42), and (44) we can eliminate q and P to find

$$\omega_0 r = -W\left[\frac{\mathrm{d}P_o}{\mathrm{d}r} - \frac{\mathrm{d}s_b}{\mathrm{d}r}\left(\frac{W_r - W}{W}\right)^{1/3} + \left(\frac{s_b W_r}{3W^{4/3}(W_r - W)^{2/3}} + \rho_w g\right)\frac{\mathrm{d}W}{\mathrm{d}r}\right] \tag{45}$$

where $\omega_0 = m_0/(2\rho_w k)$.

Equation (45) is a first-order ordinary differential equation (ODE) for $W(r)$. To put it in the standard form expected by a numerical ODE solver we solve it for $\mathrm{d}W/\mathrm{d}r$.

6.2 A nontrivial solution

Though Eq. (45) has a constant solution $W(r) = W_r$, to generate a nontrivial exact solution we will choose a positive thickness of ice at the margin (a cliff) so that $P_o(L^-) > 0$. At the ice margin $r = L$ we have water pressure $P = 0$ so $W(L) = W_c(L^-)$ is the boundary condition for the ODE. We assume that at the margin there is some sliding so that $s_b(L^-) > 0$, and by Eq. (A1) we require that $s_b(L^-)W_r > P_o(L^-)^3 W(L)$. The condition at $r = L$ also satisfies $W(L) < W_r$. Then we integrate Eq. (45) from $r = L$ to $r = 0$. The central water thickness value $W(0)$ is determined as part of the solution.

It is useful to have an ice cap geometry in which the surface gradient formula is simple so that $\mathrm{d}P_o/\mathrm{d}r$ in Eq. (45) is also simple, so we choose a parabolic profile

$$H(r) = H_0\left(1 - \frac{r^2}{R_0^2}\right) \tag{46}$$

where $H(0) = H_0$ is the height (thickness) at the center of the ice cap. It follows that $\mathrm{d}P_o/\mathrm{d}r = -Cr$ where $C = 2\rho_i g H_0 R_0^{-2}$. We choose $L = 0.9R_0$ and we note that $H(L) = 0.19H_0$ is the size of the cliff.

GMDD
7, 4705–4775, 2014

The sliding speed could be determined by a model for stresses at the ice base and within the ice (Greve and Blatter, 2009), but for hydrology model verification we simply choose a well-behaved sliding speed function which has no sliding near the ice cap center, until a radius $r = R_1$ at which sliding increases:

$$|\boldsymbol{v}_b|(r) = \begin{cases} 0, & 0 \le r \le R_1, \\ v_0 \left(\frac{r-R_1}{L-R_1}\right)^5, & R_1 < r \le L. \end{cases} \tag{47}$$

It follows from Eqs. (A2) and (47) that $\mathrm{d}s_b/\mathrm{d}r$ in Eq. (45) is bounded and continuous on $0 \le r \le L$.

Now we solve ODE Eq. (45) with initial condition $W(L)$ and the specific values in Table 3. We use adaptive numerical ODE solvers, both a Runge–Kutta 4(5) Dormand–Prince method and a variable-order stiff solver, with relative tolerance 10^{-12} and absolute tolerance 10^{-9}. The two solvers gave essentially identical results. Modest stiffness (Ascher and Petzold, 1998) of ODE Eq. (45) is observed at $r \approx R_1$. The result $W(r)$ is shown in Fig. 2.

Because Eqs. (46) and (47) imply a pressure functional relation $P = P(W, r)$ from Eq. (A4), we can also show in Fig. 2 the regions of the r, W plane which correspond to overpressure, normal pressure, and underpressure. We see that $W(r)$ is in the normal pressure region as r decreases from $r = L$ to $r = R_1$, but at $r = R_1$ the function $W(r)$ switches into the overpressure case because there is no sliding. Figure 3 shows the corresponding pressure solution $P(r) = P(W(r))$ from Eq. (A4).

The reason for stiffness near R_1 is that as the sliding goes to zero the cavitation rate goes to zero. Because creep closure balances cavitation in steady state, effective pressure also goes to zero ($P \to P_o$). The remaining active mechanisms in the model are the variable overburden pressure and the rate of water input, and they must exactly

GMDD
7, 4705–4775, 2014

balance. In this case Eq. (45) reduces to the simpler form

$$\frac{dW}{dr} = -\frac{\varphi_o r W^{-1} + \frac{dP_o}{dr}}{\rho_w g}. \tag{48}$$

Though we have not derived it this way, Eq. (48) is the steady radial form of the mass conservation equation under the "$P = P_o$" closure, namely Eq. (27).

In Eq. (48) we see that $dW/dr = 0$ if W satisfies $W = -\varpi_0 r/(dP_o/dr)$. In our case with geometry Eq. (46) this reduces to a constant value $W^* = 0.21764\,\text{m}$ because dP_o/dr is linear in r. Both numerical ODE solvers used here confirm that $W(r)$ is asymptotic to this constant value W^* as $r \to 0$, and that $W(r) \approx W^*$ within about 1 % on all of $0 \le r \le R_1$. This is seen in Fig. 2.

7 Numerical schemes

All the numerical schemes described in this section are implemented in parallel using the PETSc library (Balay et al., 2011).

7.1 Mass conservation: time-stepping

The mass conservation equation in model Eq. (34) will be discretized by an explicit, conservative finite difference method. A centered, second-order scheme will be applied to the diffusion part. Two schemes for the advection part will be compared, namely first-order upwinding and a higher-order flux-limited upwind-biased method.

We first consider stable time steps. Stability for the advection schemes occurs with a time step $\Delta t \le \Delta t_{\text{CFL}}$ where

$$\Delta t_{\text{CFL}} \left(\frac{\max|u|}{\Delta x} + \frac{\max|v|}{\Delta y} \right) = \frac{1}{2}. \tag{49}$$

GMDD
7, 4705–4775, 2014

Because of the additional diffusion process, for stability the time step should also satisfy $\Delta t \le \Delta t_W$ where (Morton and Mayers, 2005)

$$\Delta t_W \max D \left(\frac{1}{\Delta x^2} + \frac{1}{\Delta y^2} \right) = \frac{1}{4}. \tag{50}$$

The condition $\Delta t \le \min\{\Delta t_{\text{CFL}}, \Delta t_W\}$ is sufficient for stability and convergence of the scheme. We show this for the first-order upwind scheme, but standard theory suggests the same conclusion for the higher-order flux-limited advection scheme Hundsdorfer and Verwer, 2010.

We can understand the scale of these restrictions better by considering an example using the parameter values in Table 1. We ran the model on a $\Delta x = \Delta y = 250\,\text{m}$ grid to approximate steady state for the subglacial hydrology of Nordenskiöldbreen (van Pelt, 2013). We used a hypothesized water input distribution with average value about $1\,\text{m}\,\text{a}^{-1}$, and a glacier-wide constant sliding rate of $50\,\text{m}\,\text{a}^{-1}$. The result is that the maximum computed water speed $|\boldsymbol{V}|$ is about $0.2\,\text{m}\,\text{s}^{-1}$ so the advective restriction Eq. (49) is $\Delta t_{\text{CFL}} \approx 300\,\text{s} \approx 10^{-5}\,\text{a}$. Computed diffusivity $D = \rho_w g K W$ has a maximum value that varies significantly in time, $0.1 \le \max D \le 5\,\text{m}^2\,\text{s}^{-1}$. Diffusive restriction Eq. (50) using value $\max D = 1\,\text{m}^2\,\text{s}^{-1}$ is $\Delta t_W \approx 8000\,\text{s} \approx 2.5 \times 10^{-4}\,\text{a}$. Thus in this example $\Delta t_W \approx 25 \Delta t_{\text{CFL}}$.

This example suggests that, unless both the maximum velocity is unusually slow and deep subglacial lakes develop so that D is large, the diffusive time scale is significantly longer than the CFL time scale for a 250 m grid. The scaling $\Delta t_W = O(\Delta x^2)$ vs. $\Delta t_{\text{CFL}} = O(\Delta x^1)$ makes it clear that under sufficient spatial grid refinement Δt_W is the controlling restriction, but we suppose that Δt_{CFL} is controlling for $\Delta x \gg 100\,\text{m}$. We will see below, however, that the time step restriction associated to an explicit time-stepping method for the pressure equation is typically shorter than either of $\Delta t_W, \Delta t_{\text{CFL}}$, and it scales as $O(\Delta x^2)$ like Δt_W.

If implicit time-stepping is used for the pressure equation, which requires variational inequality treatment to preserve physical pressure bounds (Schoof et al., 2012), then

GMDD
7, 4705–4775, 2014

the time scales $\Delta t_W, \Delta t_{\text{CFL}}$ addressed here are the only restrictions. The time step restriction Δt_W could also be removed by implicit steps for the mass-conservation equation, though it would seem this requires another variational inequality formulation because of the lower bound $W \geq 0$. Our observation that $\Delta t_{\text{CFL}} \ll \Delta t_W$ for practical ice sheet grids suggests that implicit time-stepping for the mass-conservation equation is not beneficial.

7.2 Mass conservation: spatial discretization

To set notation, suppose the rectangular computational domain has $M_x \times M_y$ gridpoints (x_i, y_j) with uniform spacing $\Delta x, \Delta y$. Let $W^l_{i,j} \approx W(t_l, x_i, y_j)$, $(W_{\text{til}})^l_{ij} \approx W_{\text{til}}(t_l, x_i, y_j)$, and $P^l_{i,j} \approx P(t_l, x_i, y_j)$ denote the numerical approximations.

We will compute velocity components and flux components at the staggered (cell-face-centered) points shown in Fig. 4 using centered finite difference approximations of Eqs. (10) and (11). We use "compass" indices such as $u_{\text{e}} = u_{i+1/2,j}$ for the "east" staggered value of u and $v_{\text{n}} = v_{i,j+1/2}$ for the "north" staggered value of v. Similarly we use compass indices for staggered grid values of the water layer thickness, computed by averaging regular grid values:

$$W_{\text{e}} = \left(W^l_{i,j} + W^l_{i+1,j}\right)/2, \qquad (51)$$
$$W_{\text{n}} = \left(W^l_{i,j} + W^l_{i,j+1}\right)/2.$$

The nonlinear effective conductivity K from Eq. (9) is also needed at staggered locations. As a notational convenience define $R = P + \rho_{\text{w}} g b$ and define these staggered-grid

GMDD
7, 4705–4775, 2014

values (compare Mahaffy, 1976):

$$\Pi_{\mathrm{e}} = \left| \frac{R_{i+1,j} - R_{i,j}}{\Delta x} \right|^2 + \left| \frac{R_{i+1,j+1} + R_{i,j+1} - R_{i+1,j-1} - R_{i,j-1}}{4\Delta y} \right|^2,$$

$$\Pi_{\mathrm{n}} = \left| \frac{R_{i+1,j+1} + R_{i+1,j} - R_{i-1,j+1} - R_{i-1,j}}{4\Delta x} \right|^2 + \left| \frac{R_{i,j+1} - R_{i,j}}{\Delta y} \right|^2.$$

Thereby define

$$K_{\mathrm{e}} = k W_{\mathrm{e}}^{\alpha-1} \Pi_{\mathrm{e}}^{(\beta-2)/2}, \quad K_{\mathrm{n}} = k W_{\mathrm{n}}^{\alpha-1} \Pi_{\mathrm{n}}^{(\beta-2)/2}. \tag{52}$$

The velocity components are then found by differencing:

$$u_{\mathrm{e}} = -K_{\mathrm{e}} \left(\frac{P_{i+1,j} - P_{i,j}}{\Delta x} + \rho_{\mathrm{w}} g \frac{b_{i+1,j} - b_{i,j}}{\Delta x} \right), \tag{53}$$

$$v_{\mathrm{n}} = -K_{\mathrm{n}} \left(\frac{P_{i,j+1} - P_{i,j}}{\Delta y} + \rho_{\mathrm{w}} g \frac{b_{i,j+1} - b_{i,j}}{\Delta y} \right).$$

Similarly for diffusivity we have

$$D_{\mathrm{e}} = \rho_{\mathrm{w}} g K_{\mathrm{e}} W_{\mathrm{e}}, \qquad D_{\mathrm{n}} = \rho_{\mathrm{w}} g K_{\mathrm{n}} W_{\mathrm{n}}. \tag{54}$$

We get the remaining staggered-grid quantities by shifting indices:

$$u_{\mathrm{w}} = u_{\mathrm{e}}|_{(i-1,j)}, \quad K_{\mathrm{w}} = K_{\mathrm{e}}|_{(i-1,j)}, \quad D_{\mathrm{w}} = D_{\mathrm{e}}|_{(i-1,j)},$$
$$v_{\mathrm{s}} = v_{\mathrm{n}}|_{(i,j-1)}, \quad K_{\mathrm{s}} = K_{\mathrm{n}}|_{(i,j-1)}, \quad D_{\mathrm{s}} = D_{\mathrm{n}}|_{(i,j-1)}.$$

Now we define $Q_{\mathrm{e}}(u_{\mathrm{e}})$, $Q_{\mathrm{w}}(u_{\mathrm{w}})$, $Q_{\mathrm{n}}(v_{\mathrm{n}})$, and $Q_{\mathrm{s}}(v_{\mathrm{s}})$ as the face-centered (staggered-grid) normal components of the advective flux $\boldsymbol{V}W$. These quantities are described in

GMDD
7, 4705–4775, 2014

more detail in the next subsection. They use only the staggered velocity component but there is upwinding to determine which W value, or combination of W values, is used.

The grid values of $\mathcal{D} = \nabla\cdot\boldsymbol{q} = \nabla\cdot(\boldsymbol{V}W) - \nabla\cdot(D\nabla W)$ using Eqs. (53) and (54) now become:

$$\mathcal{D}_{i,j} = \frac{Q_{\mathrm{e}}(u_{\mathrm{e}}) - Q_{\mathrm{w}}(u_{\mathrm{w}})}{\Delta x} + \frac{Q_{\mathrm{n}}(v_{\mathrm{n}}) - Q_{\mathrm{s}}(v_{\mathrm{s}})}{\Delta y} - \frac{D_{\mathrm{e}}(W^l_{i+1,j} - W^l_{i,j}) - D_{\mathrm{w}}(W^l_{i,j} - W^l_{i-1,j})}{\Delta x^2} - \frac{D_{\mathrm{n}}(W^l_{i,j+1} - W^l_{i,j}) - D_{\mathrm{s}}(W^l_{i,j} - W^l_{i,j-1})}{\Delta y^2}. \tag{55}$$

To ensure conservation, $Q_{\mathrm{e}}(u_{\mathrm{e}})$ used in computing $\mathcal{D}_{i,j}$ must be the same as $Q_{\mathrm{w}}(u_{\mathrm{w}})$ used in computing $\mathcal{D}_{i+1,j}$, and similarly for "north" and "south" staggered fluxes; our formulas have these properties.

Now our scheme for approximating mass conservation Eq. (12) is

$$\frac{W^{l+1}_{i,j} - W^l_{i,j}}{\Delta t} + \frac{(W_{\mathrm{til}})^{l+1}_{i,j} - (W_{\mathrm{til}})^l_{i,j}}{\Delta t} = -\mathcal{D}_{i,j} + \frac{m_{ij}}{\rho_{\mathrm{w}}}. \tag{56}$$

The updated value of W_{til}, which appears on the left side of Eq. (56), is computed by trivial integration of Eq. (16), namely

$$(W_{\mathrm{til}})^{l+1}_{i,j} = (W_{\mathrm{til}})^l_{i,j} + \Delta t\left(\frac{m_{ij}}{\rho_{\mathrm{w}}} - C_{\mathrm{d}}\right). \tag{57}$$

The right-hand-side value is used if it is in the closed interval $[0, W^{\max}_{\mathrm{til}}]$, but otherwise the bounds $0 \le W_{\mathrm{til}} \le W^{\max}_{\mathrm{til}}$ are enforced. Once W^{l+1}_{til} is computed, the value of W^{l+1} can be updated by Eq. (56) in a mass-conserving way.

GMDD
7, 4705–4775, 2014

Assuming no error in the flux components Q, the local truncation error (Morton and Mayers, 2005) of scheme Eq. (56) would be $O(\Delta t^1 + \Delta x^2 + \Delta y^2)$ as an approximation of Eq. (12). The actual truncation error depends on the nature of the approximation which generates the discrete fluxes, next.

7.3 Discrete advective fluxes

We test two flux discretization schemes Eq. (56), namely first-order upwind and the Koren flux-limited third-order scheme (Hundsdorfer and Verwer, 2010). Both schemes achieve non-oscillation and positivity, but with different local truncation error and complexity of implementation. The third-order scheme is best explained as a modification of the better-known conservative ("donor cell"; LeVeque, 2002) first-order upwind scheme we use.

In fact, the following formulas apply in the cases $u_e \geq 0$, $u_e < 0$, $v_n \geq 0$, and $v_n < 0$, respectively:

$$Q_e(u_e) = u_e \left[W_{i,j} + \Psi(\theta_i)(W_{i+1,j} - W_{i,j}) \right], \tag{58}$$

$$Q_e(u_e) = u_e \left[W_{i+1,j} + \Psi\left((\theta_{i+1})^{-1} \right) (W_{i,j} - W_{i+1,j}) \right],$$

$$Q_n(v_n) = v_n \left[W_{i,j} + \Psi(\theta_j)(W_{i,j+1} - W_{i,j}) \right],$$

$$Q_n(v_n) = v_n \left[W_{i,j+1} + \Psi\left((\theta_{j+1})^{-1} \right) (W_{i,j} - W_{i,j+1}) \right].$$

The subscripted θ quotients are as follows:

$$\theta_i = \frac{W_{i,j} - W_{i-1,j}}{W_{i+1,j} - W_{i,j}}, \qquad (\theta_{i+1})^{-1} = \frac{W_{i+2,j} - W_{i+1,j}}{W_{i+1,j} - W_{i,j}},$$

$$\theta_j = \frac{W_{i,j} - W_{i,j-1}}{W_{i,j+1} - W_{i,j}}, \qquad (\theta_{j+1})^{-1} = \frac{W_{i,j+2} - W_{i,j+1}}{W_{i,j+1} - W_{i,j}}.$$

The first-order upwind scheme simply sets $\Psi(\theta) = 0$ in formulas Eq. (58). The Koren scheme "limits" its third-order and positive-coefficient correction to the upwind scheme

GMDD
7, 4705–4775, 2014

by using this formula (Hundsdorfer and Verwer, 2010):

$$\Psi(\theta) = \max\left\{0, \min\left\{1, \theta, \frac{1}{3} + \frac{1}{6}\theta\right\}\right\}. \tag{59}$$

When using the Koren flux-limiter the stencil in Fig. 4 is extended because regular grid neighbors $W_{i+2,j}$, $W_{i-2,j}$, $W_{i,j+2}$, $W_{i,j-2}$ are also involved in updating $W_{i,j}$. The flux-correction-limited Koren third-order scheme bypasses the first-order limitation of positive linear finite difference/volume schemes imposed by Godunov's barrier theorem (Hundsdorfer and Verwer, 2010, Sect. I.7.1) by having a nonlinear correction formula, i.e. the combination of Eqs. (58) and (59) above. Though the Koren scheme is usually third-order where smoothness allows, it reverts to first-order at extrema and other non-smooth areas where $\theta \gg 1$ or $\theta \ll 1$.

For either the first-order or Koren schemes, if the water input m is negative then we must actively enforce the positivity of the water thickness W. Positivity of the source-free advection-diffusion scheme is a desirable property but it does not ensure positivity of the solution if there is actual water removal (i.e. if $(m/\rho_w) - \partial W_{til}/\partial t < 0$). Therefore we project (reset) W to be nonnegative at the end of each time step.

7.4 Mass conservation: positivity and stability

Explicit numerical scheme Eq. (56) for the mass conservation PDE Eq. (12), combined with the first-order upwind case of formulas Eq. (58), is sufficiently simple so that we can analyze its stability properties. For this scheme we now sketch a maximum principle argument which shows stability (Morton and Mayers, 2005). The argument also shows positivity (Hundsdorfer and Verwer, 2010) as long as the total water input is nonnegative, but here only the case $m = 0$ and $W_{til}^{max} = 0$ case is shown. Also we consider only the upwinding case where the discrete velocities at cell interfaces are nonnegative: $u_e \geq 0$, $u_w \geq 0$, $v_n \geq 0$, $v_s \geq 0$. The other upwinding cases can be handled by similar arguments.

GMDD
7, 4705–4775, 2014

Define $\nu_x = \Delta t/\Delta x$, $\nu_y = \Delta t/\Delta y$, $\mu_x = \Delta t/\Delta x^2$, and $\mu_y = \Delta t/\Delta y^2$. Collecting terms in Eq. (56) to write the new value as a linear combination of the old values, we get

$$\begin{aligned} W_{i,j}^{l+1} &= (\nu_x u_w + \mu_x D_w) W_{i-1,j}^l + (\mu_x D_e) W_{i+1,j}^l \\ &\quad + (\nu_y v_s + \mu_y D_s) W_{i,j-1}^l + (\mu_y D_n) W_{i,j+1}^l \\ &\quad + \left[1 - \nu_x u_e - \nu_y v_n - \mu_x (D_e + D_w) - \mu_y (D_n + D_s)\right] W_{i,j}^l \\ &= \tilde{A} W_{i-1,j}^l + \tilde{B} W_{i+1,j}^l + \tilde{C} W_{i,j-1}^l + \tilde{D} W_{i,j+1}^l + \tilde{E} W_{i,j}^l. \end{aligned} \tag{60}$$

Because of our assumption about nonnegative velocities, and noting that the diffusivities are nonnegative, we see that coefficients $\tilde{A}, \tilde{B}, \tilde{C}, \tilde{D}$ are all nonnegative. Only $\tilde{E}$ could be negative, depending on values of ν_x, ν_y, μ_x, and μ_y.

Requiring $\tilde{E}$ in Eq. (60) to be nonnegative is a sufficient stability condition (Morton and Mayers, 2005), which we generate based on an equal split between advective and diffusive parts. First there is a CFL restriction for the advection terms, namely $\nu_x \alpha_e + \nu_y \beta_n \le \frac{1}{2}$, which is condition Eq. (49) when generalized to all upwinding cases. The second is a time-step restriction on the diffusion, namely $\mu_x (D_e + D_w) + \mu_y (D_n + D_s) \le \frac{1}{2}$, which is condition Eq. (50). If both Eqs. (49) and (50) hold then the coefficient $\tilde{E}$ in Eq. (60) is nonnegative.

Because the coefficients in linear combination Eq. (60) also add to one, as the reader may check, it follows from Eqs. (49) and (50) that the scheme is stable (Morton and Mayers, 2005). It also follows from Eqs. (49) and (50) that if $W_{i,j}^l \ge 0$ for all i, j then Eq. (60) gives $W_{ij}^{l+1} \ge 0$, in this $m = 0$ and $W_{\text{til}}^{\max} = 0$ case, which is our positivity claim. Thus, under conditions Eqs. (49) and (50), scheme Eq. (56) is stable and positivity-preserving.

GMDD
7, 4705–4775, 2014

7.5 Discretization of the pressure equation

The pressure evolution Eq. (33) is a nonlinear diffusion with additional "reaction" terms associated to opening and closing. The time step restriction for our explicit pressure scheme is comparable to Eq. (50), though the proof above for the stability of the mass conservation scheme does not suffice to prove stability. That is, if the time step satisfies $\Delta t \le \Delta t_P$, where

$$\Delta t_P \left(\frac{2 \max D}{\phi_0}\right)\left(\frac{1}{\Delta x^2} + \frac{1}{\Delta y^2}\right) = 1 \tag{61}$$

then we assert that, and observe in practice that, the scheme is stable. From Eq. (50) the resulting time step Δt_P is a fraction of Δt_W:

$$\Delta t_P = 2\phi_0 \, \Delta t_W. \tag{62}$$

We can again be quantitative in a particular example. Consider the same 250 m simulation of the hydrology of Nordenskiöldbreen as earlier. With $\phi_0 = 0.01$ we have Δt_P which is 50 times smaller than Δt_W and half of Δt_{CFL}:

$\Delta t_W \approx 8000$ s — from Eq. (50),
$\Delta t_{\text{CFL}} \approx 300$ s — from Eq. (49),
$\Delta t_P \approx 160$ s — from Eq. (62).

This analysis suggests that the numerical scheme for pressure diffusion, given next, may often have the shortest time step, but it may be comparable to CFL. Note that $\Delta t_{\text{CFL}} = O(\Delta x)$ while Δt_W and Δt_P are $O(\Delta x^2)$. The time step restriction Δt_P scales with the adjustable regularizing porosity ϕ_0 so we can make it more or less severe.

The scheme we use for the pressure Eq. (33) is similar to the scheme we have just presented for the mass continuity Eq. (12). Denote $\psi^l_{i,j} = P^l_{i,j} + \rho_{\text{w}} g(b_{i,j} + W^l_{i,j})$. Let $\mathcal{O}_{ij} = c_1 |\boldsymbol{v}_{\text{b}}|_{i,j} (W_{\text{r}} - W^l_{i,j})_+$ and $\mathcal{C}_{ij} = c_2 A (\rho_{\text{i}} g H_{i,j} - P^l_{i,j})^3 W^l_{i,j}$ be the gridded values of

GMDD
7, 4705–4775, 2014

the cavitation-opening and creep-closure rates. Also define the sum of all zero order (i.e. without spatial derivatives) terms

$$Z_{ij} = \mathcal{C}_{ij} - \mathcal{O}_{ij} + \frac{m_{ij}}{\rho_w} - \frac{(W_{til})_{ij}^{l+1} - (W_{til})_{ij}^{l}}{\Delta t}. \tag{63}$$

Using Eq. (55) for the flux divergence, the scheme for pressure Eq. (33) is now

$$\frac{\phi_0}{\rho_w g} \frac{P_{i,j}^{l+1} - P_{i,j}^{l}}{\Delta t} = -\mathcal{D}_{i,j} + Z_{ij}, \tag{64}$$

or, in explicit update form,

$$P_{i,j}^{l+1} = P_{i,j}^{l} + \frac{\rho_w g \, \Delta t}{\phi_0} \left(-\mathcal{D}_{i,j} + Z_{ij}\right). \tag{65}$$

Because Eq. (63) uses the updated value $(W_{til})_{ij}^{l+1}$, Eq. (57) must be applied before Eq. (65) can be used to update P to the new time t_{l+1}.

There are special cases at the boundaries of the active subglacial layer: (i) where there is land ($b_{i,j} > 0$) and no ice ($H_{i,j} = 0$) we set $P_{i,j}^{l+1} = 0$, (ii) where the ice is floating we set $P_{i,j}^{l+1} = (P_o)_{i,j}$, and (iii) where there is grounded ice ($H_{i,j} > 0$) and no water ($W_{i,j}^{l} = 0$) we set $P_{i,j}^{l+1} = (P_o)_{i,j}$ if there is no basal sliding and $P_{i,j}^{l+1} = 0$ if there is sliding (because of cavitation; see Eq. A4).

7.6 One time step of the model

Mathematical model Eq. (34) evolves W, W_{til}, and P. Here we describe one time step of the fully-discretized evolution. For convenience we treat the ice geometry and sliding speed as fixed, and so $h_{i,j}$, $b_{i,j}$, $(P_o)_{i,j}$, and $|\boldsymbol{v}_b|_{i,j}$ are all denoted as time-independent.

GMDD
7, 4705–4775, 2014

The ice geometry may be quite general, with ice-free land or floating ice allowed at any location (x_i, y_j). The ice geometry determines boolean "masks" for grid cell state (based on zero sea level elevation):

$$\texttt{icefree}_{i,j} = (h_{i,j} > 0) \text{ and } (h_{i,j} = b_{i,j}),$$
$$\texttt{float}_{i,j} = (\rho_{\mathrm{i}}(H_{\mathrm{float}})_{i,j} < -\rho_{\mathrm{sw}}\, b_{i,j}).$$

Here we take a sea-water density $\rho_{\mathrm{sw}} = 1028.0$ and define $H_{\mathrm{float}} = h_{i,j}/(1-r)$ as the thickness of the ice if it is floating, where $r = \rho_{\mathrm{i}}/\rho_{\mathrm{sw}}$. Note that $\texttt{float}_{i,j}$ is also true in ice-free ocean. The subglacial hydrology model exists only for grounded ice, that is, only if both `icefree` and `float` are false. The other mask cases provide boundary conditions when they are neighbors to grounded ice-filled cells.

One time step follows this algorithm:

i. Start with values $W^l_{i,j}$, $(W_{\mathrm{til}})^l_{i,j}$, $P^l_{i,j}$ which satisfy the bounds $W \ge 0$, $0 \le W_{\mathrm{til}} \le W_{\mathrm{til}}^{\mathrm{max}}$, and $0 \le P \le P_{\mathrm{o}}$.

ii. Get $(W_{\mathrm{til}})^{l+1}_{i,j}$ by Eq. (57). Enforce $0 \le W_{\mathrm{til}} \le W_{\mathrm{til}}^{\mathrm{max}}$. If $\texttt{icefree}_{i,j}$ or $\texttt{float}_{i,j}$ then set $(W_{\mathrm{til}})^{l+1}_{i,j} = 0$.

iii. Get W values averaged onto the staggered grid from Eq. (51), staggered grid values of the effective conductivity K from Eq. (52), velocity components u, v at staggered grid locations from Eq. (53), and staggered grid values of the diffusivity D from Eq. (54).

iv. Get time step $\Delta t = \min\{\Delta t_{\mathrm{CFL}}, \Delta t_W, \Delta t_P\}$ using criteria Eqs. (49), (50), and (62).

v. Using Eq. (58) and a particular flux-limiter, compute the advective fluxes $Q_{\mathrm{e}}(\alpha_{\mathrm{e}})$ at all staggered-grid points $(i+1/2, j)$ and $Q_{\mathrm{n}}(\beta_{\mathrm{n}})$ at all staggered-grid points $(i, j+1/2)$.

GMDD
7, 4705–4775, 2014

vi. Get approximations $\mathcal{D}_{i,j}$ of the flux divergence from Eq. (55). For each direction (i.e. x- and y-directions), do not compute the divided-difference contribution to the flux divergence in Eq. (55) if either neighbor is `icefree` or `float`.

vii. If $\texttt{icefree}_{i,j}$ then set $P_{i,j}^{l+1} = 0$. If $\texttt{float}_{i,j}$ then set $P_{i,j}^{l+1} = (P_o)_{i,j}$. If $W_{i,j}^{l} = 0$ and $\texttt{icefree}_{i,j}$ and $\texttt{float}_{i,j}$ are both false, then set $P_{i,j}^{l+1} = (P_o)_{i,j}$. Then use Eq. (65) to compute values for $P_{i,j}^{l+1}$ at the remaining locations.

viii. If $P_{i,j}^{l+1}$ does not satisfy bounds $0 \le P \le P_o$ then reset (project) into this range.

ix. If $\texttt{icefree}_{i,j}$ or $\texttt{float}_{i,j}$ then set $W_{i,j}^{l+1} = 0$. Otherwise use Eq. (56) to compute values for $W_{i,j}^{l+1}$.

x. If $W_{i,j}^{l+1} < 0$ then reset (project) $W_{i,j}^{l+1} = 0$.

xi. Update time $t_{l+1} = t_l + \Delta t$ and repeat at (i).

This recipe goes with a reporting scheme for mass conservation. Note that in steps (ii) and (ix) water is lost or gained at the margin where either the ice thickness goes to zero on land (margins), or at locations where the ice becomes floating (grounding lines). Because such loss/gain may be the modeling goal – users want hydrological discharge – these amounts are reported. This reporting scheme also tracks the projections in step (x), which represent a mass conservation error which goes to zero under the continuum limit $\Delta t \to 0$.

8 PISM options for hydrology models

In this section we document the runtime options for the PISM hydrology model (PISM authors, 2013). There are three choices of model equations, namely `distributed`, `routing`, and `null`. The first of these is the complete model described in this paper. The other two are reductions; we list them in order of decreasing complexity.

GMDD
7, 4705–4775, 2014

8.1 `distributed`

This most-complete PISM hydrology model is chosen by runtime option `-hydrology distributed`. It is governed by the full set of Eq. (34) in Sect. 5; see also Tables 1 and 2.

8.2 `routing`

This model is chosen by option `-hydrology routing`. It is governed by a subset of Eq. (34), with the equation for evolution of pressure P removed, and with the replacement $P \mapsto P_o = \rho_i g H$ in defining K, $\boldsymbol{V}$, and ψ. Thus the equations simplify to:

$$\frac{\partial W}{\partial t} + \frac{\partial W_{til}}{\partial t} = -\nabla\cdot(\boldsymbol{V}W) + \nabla\cdot(D\nabla W) + \frac{m}{\rho_w}, \tag{66}$$
$$\frac{\partial W_{til}}{\partial t} = \frac{m}{\rho_w} - C_d,$$

along with bounds $0 \le W$ and $0 \le W_{til} \le W_{til}^{max}$. The determination of N_{til} and τ_c is unchanged.

8.3 `null`

This non-conserving model is chosen by option `-hydrology null`. It is the default hydrology model in PISM. It has only the state variable W_{til}. It uses only evolution Eq. (16).

8.4 Configurable constants

All of the constants in Table 1 are configurable parameters in PISM. The correspondence between PISM parameters names and the symbols in this paper is in Table 4. These parameters can be changed at runtime by using the parameter name as an

GMDD
7, 4705–4775, 2014

option or by setting a `pism_overrides` variable in a NetCDF file which is read with the `-config_override` option. See `src/pism_config.cdl` for default values and units.

9 Results

9.1 Verification of the coupled model

By using the coupled steady-state exact solution constructed in Sect. 6 we can verify most of the numerical schemes described above. Verification is the process of measuring and analysing the errors made by the numerical scheme, especially as the numerical grid is refined (Wesseling, 2001; Bueler et al., 2005).

We initialize our time-stepping numerical scheme with the exact steady solution and we measure the error relative to the steady exact values after one model-month. The continuum time-dependent model Eq. (34) would cause no drift away from steady state, so any drift is error.

For the verification runs we use the values in Table 3. We do runs on grids decreasing by factors of two from 2 km to 125 m. Figure 5 shows the results based on first-order upwinding for the fluxes.

This convergence evidence suggests that the coupled advection-diffusion-reaction equations for W and P have correctly-implemented numerical schemes. The rate of convergence is roughly linear (i.e. about $O(\Delta x^1)$) because largest errors arise at locations of low regularity of the solution, including the radius $r = R_1$ where P abruptly drops from P_0, and at the ice sheet margin $r = L$ where there is a jump in the water thickness to zero.

The rates of convergence for average errors are nearly identical for the higher order flux-limited (Koren) scheme and for the first-order upwinding scheme (not shown). Because our problem is an advection-diffusion problem in which both the advection velocity and the diffusivity are solution-dependent, it is difficult to separate the errors

GMDD
7, 4705–4775, 2014

arising from numerical treatments of advection and diffusion. The first-order upwinding scheme for the advection has much larger numerical diffusivity but this diffusivity is masked by the physical diffusivity. Based on our verification evidence it is reasonable to choose the simpler first-order upwinding for applications. It also requires less interprocess communication in a parallel implementation like ours.

9.2 Application of the model at ice sheet scale

We now apply our mass-conserving hydrology models to the entire Greenland ice sheet at 2 km grid resolution. This nontrivial example demonstrates the model at large computational scale using real ice sheet geometry, with one-way coupling from ice dynamics for a realistic distribution of sliding and basal melt rate.

9.2.1 Spun-up initial state

The PISM dynamics and thermodynamics model (Bueler and Brown, 2009; Winkelmann et al., 2011; Aschwanden et al., 2012), using the non-mass-conserving `null` hydrology model (Sect. 8), was applied by grid sequencing to compute a consistent and nearly-steady model of the ice sheet, a "spun-up" initial state. Model choices for ice dynamics, including enhancement factor, sliding law power, and till friction angle, follow Aschwanden et al. (2013). The steady present-day climate of the ice sheet, especially surface mass balance and surface temperature (Ettema et al., 2009), were from the SeaRISE data set for Greenland (Bindschadler and twenty-seven others, 2013). The grid sequence was 50 ka on a 20 km grid, 20 ka on a 10 km grid, 2 ka on a 5 km grid, and finally 200 a on a 2 km grid. All model fields were bilinearly interpolated at each refinement stage. This whole spinup used 2800 processor-hours on 72 processors on a linux cluster with 2.2 GHz AMD Opteron processors, a small computation for modern supercomputers.

The final 2 km stage, on a horizontal grid of 1.05 million grid points, used uniform 10 m vertical spacing so that the ice sheet flow was modelled on a structured 3-D

GMDD
7, 4705–4775, 2014

grid of 460 million grid points (e.g. locations where ice temperature and velocity were computed). In the last 100 a of the final stage the ice sheet volume varied by less than 0.04 %. Other more active measures showed stability during the last 100 a at the level of less than one percent (e.g. the area of temperate base and the maximum ice velocity over the whole sheet) to at most a few percent (the floating ice area).

The results of this whole-ice-sheet spinup were validated by comparing results to present-day observations. (Though the model is in nearly steady state, the actual Greenland ice sheet may not be as close to steady.) The spun-up ice sheet volume of $3.094 \times 10^6\,\mathrm{km}^3$ is close to the present-day volume of $3.088 \times 10^6\,\mathrm{km}^3$ computed from the SeaRISE data on the same grid. However, in describing more careful validation measures for similar 2 km PISM model runs, Aschwanden et al. (2013) observe that volume alone is inadequate for model validation. A better evaluation of dynamical quality is shown in Fig. 6, which compares the modeled and observed surface speed. We see that the extent of the Northeast Greenland ice stream is smaller than observed, and the distribution of flow in Western Greenland outlet glaciers differs from the observed pattern. Our model uses no spatially-variable parameter values such as basal shear stresses found by inversion of surface velocities.

The spun-up initial state includes, in particular, modelled ice thickness H, basal melt rate m, and sliding velocity $|\boldsymbol{v}_b|$; the latter two fields are shown in Fig. 7. We note that the areas of sliding roughly coincide with areas of basal melt because modeled basal resistance comes from the yield stress parameterized in Sect. 3.

9.2.2 Experimental setup

We used fields H, m, $|\boldsymbol{v}_b|$ from the spun-up state as steady data in five model-year runs of our mass-conserving hydrology `routing` and `distributed` models. Because these fields were fixed, only one-way coupling was tested: a steady ice dynamics model fed its fields to an evolving subglacial hydrology model. The hydrology model was initialized with the W_{til} values from the spun-up state, but with $W = 0$ initial values and $P = 0$ initial values (for `distributed`).

GMDD
7, 4705–4775, 2014

These runs had 1.05 million subglacial hydrology grid points at which variables W, W_{til}, and P were recomputed at each time-step according to the numerical model described in Sect. 7. In both `routing` and `distributed` models the modelled hydrological system became quite steady after the first three model years.

The adaptively-determined time-steps for the hydrology model reached a steady level of 4 model hours for the `routing` model based on maximum subglacial water speeds $|\boldsymbol{V}|$ of $0.05\,\mathrm{m\,s^{-1}}$ and maximum diffusivity D of $10.6\,\mathrm{m^2\,s^{-1}}$. For the `distributed` model the time steps were actually slightly longer, primarily because `routing` concentrates large water amounts and fluxes along steepest-descent paths. The time steps were about 6 model hours based on speeds $|\boldsymbol{V}|$ of $0.03\,\mathrm{m\,s^{-1}}$ and smaller maximum diffusivities D of about $0.25\,\mathrm{m^2\,s^{-1}}$. (Higher water velocities $\boldsymbol{V}$ were seen in the 250 m grid resolution Nordenskiöldbreen case mentioned in Sect. 7, based on additional simulated surface water input added to the thermodynamically-generated basal melt rate (van Pelt, 2013), and the pressure time steps in that case were shorter than the mass time steps.)

9.2.3 `routing` results

The final values of W_{til} and W for the `routing` run are shown in Fig. 8. We see that the till is fully saturated ($W_{til} = 2\,\mathrm{m}$) in essentially all areas where basal melt occurs. In the outlet glacier areas the transportable water W concentrates along curves of steepest descent of the hydraulic potential; this effect is seen in detail in Fig. 9. The grid resolution of 2 km, while very high for contemporary ice dynamics models, still represents a significant spatial "smearing" of the flow pathways. Specifically, though relatively few areas have $W > 1\,\mathrm{m}$, the continuum limit of the model would be expected to have $W \gg 1\,\mathrm{m}$ in concentrated pathways of a few meters to tens of meters width.

This model could be regarded as a minimal "conduit-like" description of the subglacial flow, because of these concentrated pathways. As noted in the introduction, however, our model has no "R-channel" conduit mechanism, in which dissipation heating of the flowing water generates wall melt-back. The location of pathways here is determined

GMDD
7, 4705–4775, 2014

primarily by the bedrock elevation detail provided by the SeaRISE data set, which is limited; the results are especially suspect in the Eastern outlet glaciers in Fig. 9.

9.2.4 `distributed` results

The final values of W and the relative water pressure P/P_o for the five model-year `distributed` run are shown in Fig. 10. Again the till is full ($W_{til} = 2\,\text{m}$) in essentially all areas where basal melt occurs, and indeed W_{til} is not shown because it is identical to that in the `routing` model in this one-way coupled case.

Recall that $|\boldsymbol{v}_b|$ determines the pressure drop caused by cavitation. The effect is to spread out the water W relative to the `routing` model, as clearly seen in Fig. 10. There is no strong concentration of W along curves of steepest descent of the hydraulic potential. This result depends, however, on the opening and closing parameters in the `distributed` model, especially parameters c_1, c_2, ϕ_0, W_r; see Tables 1 and 4. Darcy flux model parameters α, β, k are also important. Parameter identification using observed surface data, though needed, is beyond our current scope.

We can examine the local relationship between water amount W and pressure P in the `distributed` results. Though the model is near steady state, the basal melt rate, sliding speed, and overburden pressure all show the large spatial variations which are characteristic of a real ice sheet. Figure 11 shows that if we "bin" pairs (W, P) by relatively-narrow sliding velocity ranges, as shown in each scatter plot, then there is usually a rough increasing relationship between W and the relative pressure P/P_o. At fast-sliding locations the water amount is often comparable to the bed roughness scale W_r. For low sliding velocities we see generally lower water amounts ($W \lesssim W_r/10$) but a full range of pressures. In thick ice the pressure P is close to overburden even if there is fast sliding. Locations with high sliding, high water amount, and low pressure also have low ice thickness. Note Fig. 11 would show even more scatter if the run were not close to steady state, for example if there were time-varying surface melt input into the subglacier (van Pelt, 2013).

GMDD
7, 4705–4775, 2014

10 Conclusions

This paper documents additions made to the Parallel Ice Sheet Model in its 0.6 version released February 2014. It describes and demonstrates a subglacial hydrology model which is novel in having these features:

- a 2-D parallel implementation of a coupled till-and-linked-cavities model (Sects. 2–7),
- an englacial porosity regularization which allows a practical numerical model in which physical bounds $0 \le P \le P_0$ hold at all times (Sects. 4 and 7),
- an analysis of steady states (Sect. 5.3 and Appendix A), describing the actual diffusivity of the advective flux in that case,
- an exact solution of the coupled mass and pressure equations in the steady radial case (Sect. 6), leading to verification (Sect. 9), and
- demonstration at whole ice-sheet scale on a million-point hydrology grid (Sect. 9).

The comprehensive treatment here of certain subjects is also important. We have

- clarified the relationship of several "closures" which turn morphological ideas about the subglacial aquifer into concrete pressure equations (Sect. 4), and
- created and implemented a common extension of several seemly-disparate published models (Sect. 5).

A deliberate limitation in scope of the current paper is that we show only one-way coupling. In this paper the PISM ice flow and thermodynamics model feeds basal melt rate and sliding velocities to the hydrology model. Two-way coupling will appear in future work.

GMDD
7, 4705–4775, 2014

Appendix A: Analysis of steady states

Relative to the time-dependent form Eq. (34), steady-state Eqs. (38)–(41) have separate balances between the divergence of the flux and the water input (Eq. 40), and the opening and closing processes (Eq. 41).

Equation (41) allows us to write the pressure $P = P(W)$ in steady state as a continuous function of the water amount W. Steady state is only possible if a condition holds:

$$c_1 |\boldsymbol{v}_\mathrm{b}| (W_\mathrm{r} - W)_+ \le c_2 A \, P_\mathrm{o}^3 W. \tag{A1}$$

That is, the maximum closing rate $C(N, W)$, which occurs at zero water pressure, must match the opening rate $\mathcal{O}(|\boldsymbol{v}_\mathrm{b}|, W)$, which is pressure-independent. Define the following scaled basal sliding speed which has units of pressure; it is a scale for the pressure drop caused by cavitation:

$$s_\mathrm{b} = \left(\frac{c_1 |\boldsymbol{v}_\mathrm{b}|}{c_2 A} \right)^{1/3}. \tag{A2}$$

Then Eq. (A1) is equivalent to

$$W \ge W_\mathrm{c} := \frac{s_\mathrm{b}^3}{s_\mathrm{b}^3 + P_\mathrm{o}^3} W_\mathrm{r}. \tag{A3}$$

If Eqs. (A1) or (A3) holds then

$$P(W) = P_\mathrm{o} - s_\mathrm{b} \left(\frac{(W_\mathrm{r} - W)_+}{W} \right)^{1/3}. \tag{A4}$$

Note that in Eq. (A4) we have $P(W_\mathrm{c}) = 0$. Underpressure ($P = 0$) with subcritical water amount ($W < W_\mathrm{c}$) does not occur in steady state though it can occur in nonsteady

GMDD
7, 4705–4775, 2014

conditions. Equation (A4) may apply even if $W \geq W_r$, in which case the water pressure takes the overburden value $P = P_o$.

Figure A1 shows the function $P(W)$ from Eq. (A4) for different values of sliding speed $|\boldsymbol{v}_b|$, and Fig. A2 shows the function for values of overburden pressure P_o. We see that as the water amount reaches the roughness scale ($W \nearrow W_r$) the pressure rises rapidly to overburden ($P(W) \nearrow P_o$). At the other extreme, we see that $P(W) \searrow 0$ as $W \searrow W_c$. The curves $P(W)$ in Figs. A1 and A2 do not include the underpressure cases $0 \leq W < W_c$ wherein Eq. (A3) is violated.

Recall that Flowers and Clarke (2002a) propose function $P_{FC}(W)$ for both steady and nonsteady circumstances. Both functions $P(W)$ in Eq. (A4) and $P_{FC}(W)$ in Eq. (29) are increasing. They both relate the water pressure to the overburden pressure P_o. However, while in Eq. (A4) the relation to P_o is additive, in Eq. (29) it is a multiplicative scaling. The power law form Eq. (29) is not justified by the physical reasoning which led to Eq. (A4), even in steady state. It would appear that any functional relationship $P(W)$ should also depend on the sliding velocity, as it does here, if cavitation influences the water pressure. Also, the $W > W_{crit}$ case gives $P_{FC}(W) > P_o$ in Eq. (29), but this condition does not arise in Eq. (A4). In the current paper is that we do not set a relationship $P = P(W)$ at all, even though such a relation emerges in runs with steady state inputs.

We now consider how the steady state water velocity $\boldsymbol{V}$, and the associated flux $\boldsymbol{q}$, depends on other quantities. Because $\boldsymbol{V}$ depends on ∇P, according to Eqs. (38) and (A4) in steady state we have

$$\frac{\partial P}{\partial W} = \frac{s_b W_r}{3W^{4/3}(W_r - W)^{2/3}} \tag{A5}$$

if $W_c < W < W_r$. If $W \leq W_c$ then $\partial P/\partial W$ is undefined, and if $W > W_r$ then $\partial P/\partial W = 0$. Note that the condition $W_c < W < W_r$ corresponds to the pressure condition $0 < P < P_o$ in steady state. Equation (A5) and Figs. A1 and A2 agree that $\partial P/\partial W \to \infty$ as $W \nearrow W_r$.

GMDD
7, 4705–4775, 2014

Equations (38), (A4), and (A5) imply a formula for the velocity in steady state:

$$\boldsymbol{V} = -k\left[\nabla\psi_{\mathrm{o}} - \left(\frac{W_{\mathrm{r}}-W}{W}\right)^{1/3}\nabla s_{\mathrm{b}} + \frac{s_{\mathrm{b}}W_{\mathrm{r}}}{3W^{4/3}(W_{\mathrm{r}}-W)^{2/3}}\nabla W\right], \tag{A6}$$

where $\psi_{\mathrm{o}} = P_{\mathrm{o}} + \rho_{\mathrm{w}} g b$. Equation (A6) helps us understand the advective flux "$\boldsymbol{V}W$" in $\boldsymbol{q}$. The direction of water velocity $\boldsymbol{V}$ is determined by a combination of a geometric direction ($\nabla\psi_{\mathrm{o}}$), a direction derived from spatial variations in the sliding speed (∇s_{b}), and a diffusive direction (∇W). Thus a portion of $\boldsymbol{V}W$ is diffusive in steady state, in addition to the *a priori* diffusive flux $-D\nabla W$. In fact we can write the whole flux as a linear combination of gradients,

$$\boldsymbol{q} = -kA_1\nabla\psi_{\mathrm{o}} + kA_2\nabla s_{\mathrm{b}} - kA_3\nabla W, \tag{A7}$$

with coefficients

$$A_1 = W, \tag{A8}$$

$$A_2 = (W_{\mathrm{r}}-W)^{1/3}W^{2/3},$$

$$A_3 = \frac{s_{\mathrm{b}}W_{\mathrm{r}}}{3(W_{\mathrm{r}}-W)^{2/3}W^{1/3}} + \rho_{\mathrm{w}} g W.$$

The first two coefficients A_1, A_2 go to zero as $W \to 0$, but A_3 remains large when $W \to 0$ as long as sliding is occurring ($s_{\mathrm{b}} > 0$). Thus for low water amount and sustained sliding we should think of the water as diffusing in the layer. When the water thickness is greater, namely if it is almost at the roughness scale ($W \lesssim W_{\mathrm{r}}$), then A_3 is large in sliding cases ($s_{\mathrm{b}} > 0$); again the effect is diffusive.

In steady state the water amount W roughly scales with $1/k$ where k is the hydraulic conductivity. In fact, if we combine Eq. (40) with Eq. (A7) and rearrange slightly then we find

$$-\nabla\cdot(A_3\nabla W) = \frac{m}{k\rho_{\mathrm{w}}} + \nabla\cdot(A_1\nabla\psi_{\mathrm{o}}) - \nabla\cdot(A_2\nabla s_{\mathrm{b}}). \tag{A9}$$

GMDD
7, 4705–4775, 2014

One may regard Eq. (A9) as a non-linear elliptic equation for W. In fact, in the case where H, b, and $|\boldsymbol{v}_b|$ are all spatially-uniform, so that $\nabla\psi_o = \nabla s_b = 0$, Eq. (A9) is of the form $-\nabla\cdot(A_3(W)\nabla W) = m/(k\rho_w)$ where $A_3(W) = A_3$ is given in Eq. (A8). If W is both bounded away from zero and bounded away from the roughness scale W_r (i.e. there is $\epsilon > 0$ so that $\epsilon < W < W_r - \epsilon$) then this equation is uniformly elliptic. Thus a maximum principle applies (Evans, 1998). This means that the maximum of W will equal or exceed the maximum of W along the boundary of that region, so the graph of W is concave down. Thus the values of W will scale with $1/k$. Indeed, for the simpler equation $-\nabla\cdot(D_0\nabla W) = m_0/(k\rho_w)$, with D_0, m_0 positive constants, on a disc of radius L, and zero boundary values, the solution has maximum value $W(0)$ which precisely scales as $1/k$. As seen in numerical results, the solution W of Eq. (A9) will also scale with $1/k$ if $\nabla\psi_o$ and ∇s_b are not too large. However, if $W \approx 0$ or $W \lesssim W_r$ then the diffusivity coefficient $A_3(W)$ will be large and so the values of W away from the boundary will be flattened-out by the resulting fast diffusion.

Acknowledgements. The first author was supported by NASA grant #NNX13AM16G. This work was supported by a grant of high-performance computing resources from the Arctic Region Supercomputing Center. Constantine Khroulev helped with the PISM implementation. Detailed comments by Andy Aschwanden, Tim Bartholomaus, and Martin Truffer were much appreciated.

References

Ascher, U. and Petzold, L.: Computer Methods for Ordinary Differential Equations and Differential-algebraic Equations, SIAM Press, Philadelphia, PA, 1998. 4723, 4730

Aschwanden, A., Bueler, E., Khroulev, C., and Blatter, H.: An enthalpy formulation for glaciers and ice sheets, J. Glaciol., 58, 441–457, doi:10.3189/2012JoG11J088, 2012. 4710, 4745

Aschwanden, A., Aðalgeirsdóttir, G., and Khroulev, C.: Hindcasting to measure ice sheet model sensitivity to initial states, The Cryosphere, 7, 1083–1093, doi:10.5194/tc-7-1083-2013, 2013. 4718, 4745, 4746

GMDD

7, 4705–4775, 2014

Balay, S., Abhyankar, S., Adams, M. F., Brown, J., Brune, P., Buschelman, K., Eijkhout, V., Gropp, W. D., Kaushik, D., Knepley, M. G., McInnes, C. L., and Rupp, K., and Smith, B. F., and Zhang, H.: PETSc Users Manual, Tech. Rep. ANL-95/11 – Revision 3.2, Argonne National Laboratory, 2011. 4731

Bartholomaus, T. C., Anderson, R. S., and Anderson, S. P.: Response of glacier basal motion to transient water storage, Nat. Geosci., 1, 33–37, doi:10.1038/ngeo.2007.52, 2008. 4722

Bartholomaus, T. C., Anderson, R. S., and Anderson, S. P.: Growth and collapse of the distributed subglacial hydrologic system of Kennicott Glacier, Alaska, USA, and its effects on basal motion, J. Glaciol., 57, 985–1002, 2011. 4706, 4707, 4711, 4714, 4721, 4722, 4726

Bindschadler, R. A., Nowicki, S., Abe-Ouchi, A., Aschwanden, A., Choi, H., Fastook, J., Granzow, G., Greve, R., Gutowski, G., Herzfeld, U., Jackson, C., Johnson, J., Khroulev, C., Levermann, A., Lipscomb, W. H., Martin, M. A., Morlighem, M., Parizek, B. R., Pollard, D., Price, S. F., Ren, D., Saito, F., Sato, T., Seddik, H., Seroussi, H., Takahashi, K., Walker, R., and Wang, W. L.: Ice-sheet model sensitivities to environmental forcing and their use in projecting future sea-level (The SeaRISE Project), J. Glaciol, 59, 195–224, 2013. 4745

Bueler, E.: Correspondence: extensions of the lumped subglacial-englacial hydrology model of Bartholomaus, et al. (2011), J. Glaciol., submitted, 2014. 4722, 4726

Bueler, E. and Brown, J.: Shallow shelf approximation as a "sliding law" in a thermodynamically coupled ice sheet model, J. Geophys. Res., 114, f03008, doi:10.1029/2008JF001179, 2009. 4715, 4717, 4718, 4726, 4745, 4759

Bueler, E., Lingle, C. S., Kallen-Brown, J. A., Covey, D. N., and Bowman, L. N.: Exact solutions and numerical verification for isothermal ice sheets, J. Glaciol., 51, 291–306, 2005. 4744

Clarke, G. K. C.: Hydraulics of subglacial outburst floods: new insights from the Spring–Hutter formulation, J. Glaciol., 49, 299–313, doi:10.3189/172756503781830728, 2003. 4723

Clarke, G. K. C.: Subglacial processes, Annu. Rev. Earth Pl. Sc., 33, 247–276, doi:10.1146/annurev.earth.33.092203.122621, 2005. 4707, 4710, 4711, 4712, 4713

Creyts, T. and Schoof, C.: Drainage through subglacial water sheets, J. Geophys. Res., 114, F04008, doi:10.1029/2008JF001215, 2009. 4706, 4708, 4712

Cuffey, K. M. and Paterson, W. S. B.: The Physics of Glaciers, 4th edn., Elsevier, 2010. 4716, 4718

Das, S. B., Joughin, I., Behn, M. D., Howat, I. M., King, M. A., Lizarralde, D., and Bhatia, M. P.: Fracture propagation to the base of the Greenland ice sheet during supraglacial lake drainage, Science, 320, 778–781, doi:10.1126/science.1153360, 2008. 4722

GMDD
7, 4705–4775, 2014

de Fleurian, B., Gagliardini, O., Zwinger, T., Durand, G., Le Meur, E., Mair, D., and Råback, P.: A double continuum hydrological model for glacier applications, The Cryosphere, 8, 137–153, doi:10.5194/tc-8-137-2014, 2014. 4707, 4708

Ettema, J., van den Broeke, M. R., van Meijgaard, E., van de Berg, W. J., Bamber, J. L., and Box, J. E., and Bales, R. C.: Higher surface mass balance of the Greenland ice sheet revealed by high-resolution climate modeling, Geophys. Res. Lett., 36, L12501, doi:10.1029/2009GL038110, 2009. 4745

Evans, L. C.: Partial Differential Equations, Graduate Studies in Mathematics, American Mathematical Society, 1998. 4720, 4753

Flowers, G. E. and Clarke, G. K. C.: A multicomponent coupled model of glacier hydrology 1. Theory and synthetic examples, J. Geophys. Res., 107, 2287, doi:10.1029/2001JB001122, 2002a. 4707, 4708, 4709, 4720, 4722, 4726, 4751

Flowers, G. E. and Clarke, G. K. C.: A multicomponent coupled model of glacier hydrology 2. Application to Trapridge Glacier, Yukon, Canada, J. Geophys. Res., 107, 2288, doi:10.1029/2001JB001124, 2002b. 4721

Fountain, A. G., Jacobel, R. W., Schlichting, R., and Jansson, P.: Fractures as the main pathways of water flow in temperate glaciers, Nature 433, 618–621, doi:10.1038/nature03296, 2005. 4722

Goeller, S., Thoma, M., Grosfeld, K., and Miller, H.: A balanced water layer concept for subglacial hydrology in large-scale ice sheet models, The Cryosphere, 7, 1095–1106, doi:10.5194/tc-7-1095-2013, 2013. 4710

Greve, R. and Blatter, H.: Dynamics of ice sheets and glaciers, in: Advances in Geophysical and Environmental Mechanics and Mathematics, Springer, 2009. 4711, 4730, 4759

Harper, J., Bradford, J., Humphrey, N., and Meierbachtol, T.: Vertical extension of the subglacial drainage system into basal crevasses, Nature, 467, 579–582, doi:10.1038/nature09398, 2010. 4707, 4722

Hewitt, I. J.: Modelling distributed and channelized subglacial drainage: the spacing of channels, J. Glaciol., 57, 302–314, 2011. 4707, 4712, 4714

Hewitt, I. J.: Seasonal changes in ice sheet motion due to melt water lubrication, Earth Planet. Sc. Lett., 371–372, 16–25, doi:10.1016/j.epsl.2013.04.022, 2013. 4707, 4708, 4712, 4722, 4723, 4727

GMDD
7, 4705–4775, 2014

Hewitt, I. J., Schoof, C., and Werder, M. A.: Flotation and free surface flow in a model for subglacial drainage. Part II: Channel flow, J. Fluid Mech., 702, 157–188, 2012. 4708, 4710, 4712, 4720, 4721, 4722, 4726, 4759

Hooke, R., Le, B., Hanson, B., Iverson, N. R., Jansson, P., and Fischer, U. H.: Rheology of till beneath Störglaciaren, Sweden, J. Glaciol., 43, 172–179, 1997. 4708, 4716, 4718

Hundsdorfer, W. and Verwer, J. G.: Numerical Solution of Time-Dependent Advection-Diffusion-Reaction Equations, Springer Series in Computational Mathematics, Springer, 2010. 4732, 4736, 4737

Huybrechts, P., Payne, T., and the EISMINT Intercomparison Group: The EISMINT benchmarks for testing ice-sheet models, Ann. Glaciol., 23, 1–12, 1996. 4759

Johnson, J. and Fastook, J. L.: Northern Hemisphere glaciation and its sensitivity to basal melt water, Quatern. Int., 95, 65–74, 2002. 4726

Kamb, B.: Glacier surge mechanism based on linked cavity configuration of the basal water conduit system, J. Geophys. Res., 92, 9083–9100, 1987. 4706, 4715

Kamb, B.: Rheological nonlinearity and flow instability in the deforming bed mechanism of ice stream motion, J. Geophys. Res.-Solid, 96, 16585–16595, 1991. 4708

Kinderlehrer, D. and Stampacchia, G.: An introduction to variational inequalities and their applications, in: Pure and Applied Mathematics, Academic Press, 1980. 4723

Le Brocq, A., Payne, A., Siegert, M., and Alley, R.: A subglacial water-flow model for West Antarctica, J. Glaciol., 55, 879–888, doi:10.3189/002214309790152564, 2009. 4711, 4719, 4720

LeVeque, R. J.: Finite volume methods for hyperbolic problems, in: Cambridge Texts in Applied Mathematics, Cambridge University Press, 2002. 4736

Lingle, C. S. and Brown, T. J.: A subglacial aquifer bed model and water pressure-dependent basal sliding relationship for a West Antarctic ice stream, in: Dynamics of the West Antarctic Ice Sheet, edited by: der Veen, C. J. V. and Oerlemans, J., D., Reidel, 1987. 4715

Livingstone, S. J., Clark, C. D., Woodward, J., and Kingslake, J.: Potential subglacial lake locations and meltwater drainage pathways beneath the Antarctic and Greenland ice sheets, The Cryosphere, 7, 1721–1740, doi:10.5194/tc-7-1721-2013, 2013. 4719, 4720, 4725

Mahaffy, M. W.: A three–dimensional numerical model of ice sheets: tests on the Barnes Ice Cap, Northwest Territories, J. Geophys. Res., 81, 1059–1066, 1976. 4734

Martin, M. A., Winkelmann, R., Haseloff, M., Albrecht, T., Bueler, E., Khroulev, C., and Levermann, A.: The Potsdam Parallel Ice Sheet Model (PISM-PIK) – Part 2: Dynamic equilibrium

GMDD
7, 4705–4775, 2014

simulation of the Antarctic ice sheet, The Cryosphere, 5, 727–740, doi:10.5194/tc-5-727-2011, 2011. 4718
Morton, K. W. and Mayers, D. F.: Numerical Solutions of Partial Differential Equations: An Introduction, 2nd edn., Cambridge University Press, 2005. 4732, 4736, 4737, 4738
Nye, J. F.: Water flow in glaciers: Jökulhlaups, tunnels and veins, J. Glaciol., 17, 181–207, 1976. 4706
Pimentel, S. and Flowers, G.: A numerical study of hydrologically driven glacier dynamics and subglacial flooding, P. Roy. Soc. A, 467, 537–558, doi:10.1098/rspa.2010.0211, 2011. 4708, 4721, 4726
Pimentel, S., Flowers, G., and Schoof, C.: A hydrologically coupled higher-order flow-band model of ice dynamics with a Coulomb friction sliding law, J. Geophys. Res., 115, F04023, doi:10.1029/2009JF001621, 2010. 4721
PISM authors: PISM, a Parallel Ice Sheet Model: User's Manual, available at: http://www.pism-docs.org (last access: 23 July 2014), 2013. 4709, 4742
Rooney, S. T., Blankenship, D. D., Alley, R. B., and Bentley, C. R.: Till beneath ice stream B: 2. structure and continuity, J. Geophys. Res.-Solid, 92, 8913–8920, 1987. 4718
Schoof, C.: The effect of cavitation on glacier sliding, P. Roy. Soc. A, 461, 609–627, doi:10.1098/rspa.2004.1350, 2005. 4707
Schoof, C.: A variational approach to ice stream flow, J. Fluid Mech., 556, 227–251, 2006a. 4718
Schoof, C.: Variational methods for glacier flow over plastic till, J. Fluid Mech., 555, 299–320, 2006b. 4708, 4716
Schoof, C.: Cavitation on deformable glacier beds, SIAM J. Appl. Math., 67, 1633–1653, 2007. 4707
Schoof, C.: Coulomb friction and other sliding laws in a higher order glacier flow model, Math. Mod. Meth. Appl. S., 20, 157–189, doi:10.1142/S0218202510004180, 2010a. 4718
Schoof, C.: Ice sheet acceleration driven by melt supply variability, Nature, 468, 803–806, 2010b. 4708, 4726, 4727
Schoof, C., Hewitt, I. J., and Werder, M. A.: Flotation and free surface flow in a model for subglacial drainage. Part I: Distributed drainage, J. Fluid Mech., 702, 126–156, 2012. 4706, 4708, 4711, 4712, 4714, 4721, 4722, 4723, 4725, 4727, 4728, 4732, 4759
Shreve, R.: Movement of water in glaciers, J. Glaciol, 11, 205–214, 1972. 4710, 4719

GMDD
7, 4705–4775, 2014

Siegert, M., Le Brocq, A., and Payne, A.: Hydrological Connections Between Antarctic Subglacial Lakes, the Flow of Water Beneath the East Antarctic Ice Sheet and Implications for Sedimentary Processes, Wiley-Blackwell, 3–10, 2009. 4719, 4725

Truffer, M. and Harrison, W.: In situ measurements of till deformation and water pressure, J. Glaciol., 52, 175–182, 2006. 4708

Truffer, M., Echelmeyer, K., and Harrison, W.: Glacier motion dominated by processes deep in underlying till, J. Glaciol., 46, 213–221, 2000. 4708, 4716

Truffer, M., Echelmeyer, K., and Harrison, W.: Implications of till deformation on glacier dynamics, J. Glaciol., 47, 123–134, doi:10.3189/172756501781832449, 2001. 4708, 4715

Tulaczyk, S., Kamb, W. B., and Engelhardt, H. F.: Basal mechanics of Ice Stream B, West Antarctica 1. Till mechanics, J. Geophys. Res., 105, 463–481, 2000a. 4707, 4708, 4715, 4716, 4718, 4759

Tulaczyk, S., Kamb, W. B., and Engelhardt, H. F.: Basal mechanics of Ice Stream B, West Antarctica 2. Undrained plastic bed model, J. Geophys. Res., 105, 483–494, 2000b. 4706, 4707, 4709, 4715, 4726

van der Wel, N., Christoffersen, P., and Bougamont, M.: The influence of subglacial hydrology on the flow of Kamb Ice Stream, West Antarctica, J. Geophys. Res.-Earth, 118, 1–14, doi:10.1029/2012JF002570, 2013. 4707, 4708, 4716, 4727

van Pelt, W.: Modelling the dynamics and boundary processes of Svalbard glaciers, Ph. D. thesis, Institute for Marine and Atmospheric Research Utrecht (IMAU), the Netherlands, 2013. 4710, 4723, 4732, 4747, 4748

Vázquez, J. L.: The Porous Medium Equation, Oxford Mathematical Monographs, The Clarendon Press Oxford University Press, Oxford, 2007. 4721

Walder, J. S.: Stability of sheet flow of water beneath temperate glaciers and implications for glacier surging, J. Glaciol., 28, 273–293, 1982. 4708

Werder, M., Hewitt, I., Schoof, C., and Flowers, G.: Modeling channelized and distributed subglacial drainage in two dimensions, J. Geophys. Res.-Earth, 118, 2140–2158, 2013. 4707, 4708, 4721, 4722, 4723, 4727

Wesseling, P.: Principles of Computational Fluid Dynamics, Springer-Verlag, 2001. 4744

Winkelmann, R., Martin, M. A., Haseloff, M., Albrecht, T., Bueler, E., Khroulev, C., and Levermann, A.: The Potsdam Parallel Ice Sheet Model (PISM-PIK) – Part 1: Model description, The Cryosphere, 5, 715–726, doi:10.5194/tc-5-715-2011, 2011. 4745

GMDD
7, 4705–4775, 2014

Table 1. Physical constants and model parameters. All values are configurable in PISM.

Name	Default	Units	Description
A	3.1689×10^{-24}	$\mathrm{Pa}^{-3}\,\mathrm{s}^{-1}$	ice softness (Huybrechts et al., 1996)
α	5/4		power in flux formula (Schoof et al., 2012)
β	3/2		power in flux formula (Schoof et al., 2012)
c_0	0	Pa	till cohesion (Tulaczyk et al., 2000a)
c_1	0.5	m^{-1}	cavitation coefficient (Schoof et al., 2012)
c_2	0.04		creep closure coefficient
C_c	0.12		till compressibility (Tulaczyk et al., 2000a)
C_d	0.001	$\mathrm{m\,a}^{-1}$	background till drainage rate
δ	0.02		N_{til} lower bound, as fraction of overburden pressure
e_0	0.69		reference void ratio at N_0 (Tulaczyk et al., 2000a)
ϕ_0	0.01		notional (regularizing) englacial porosity
g	9.81	$\mathrm{m\,s}^{-2}$	acceleration of gravity
k	0.001	$\mathrm{m}^{2\beta-\alpha}\,\mathrm{s}^{2\beta-3}\,\mathrm{kg}^{1-\beta}$	conductivity coefficient (Schoof et al., 2012)
N_0	1000	Pa	reference effective pressure (Tulaczyk et al., 2000a)
ρ_i	910	$\mathrm{kg\,m}^{-3}$	ice density (Greve and Blatter, 2009)
ρ_w	1000	$\mathrm{kg\,m}^{-3}$	fresh water density (Greve and Blatter, 2009)
W_r	0.1	m	roughness scale (Hewitt et al., 2012)
W_{til}^{max}	2	m	maximum water in till (Bueler and Brown, 2009)

GMDD
7, 4705–4775, 2014

Table 2. Functions used in subglacial hydrology model Eq. (34).

Type	Description (symbol, units, meaning)		
state	W	m	transportable water thickness
	W_{til}	m	till-stored water thickness
	P	Pa	transportable water pressure
input	b	m	bedrock elevation
	φ		till friction angle
	H	m	ice thickness
	m	$\text{kg m}^{-2}\,\text{s}^{-1}$	total melt water input
	$\lvert \boldsymbol{v}_{\text{b}} \rvert$	m s^{-1}	ice sliding speed
output	N_{til}	Pa	till effective pressure
	τ_{c}	Pa	till yield stress

GMDD
7, 4705–4775, 2014

Table 3. Constants used in constructing the exact solution.

Name	Value	Units	Description
α	1		power in flux
β	2		power in flux
H_0	500	m	center thickness
k	$0.01/(\rho_w g)$	$m^3\,s\,kg^{-1}$	hydraulic conductivity
L	22.5	km	cliff at $r = 0.9R_0$
m_0	$0.2\rho_w$	$kg\,m^{-2}\,a^{-1}$	water input rate
R_0	25	km	ideal ice cap radius
R_1	5	km	sliding starts
v_0	100	$m\,a^{-1}$	sliding speed scale
W_r	1	m	roughness scale

GMDD
7, 4705–4775, 2014

Table 4. Correspondence between symbols in this paper and PISM configuration parameter names. Alphabetical by parameter name. All of these are used in the `distributed` model, with the indicated subsets also used in the `routing` and `null` models.

PISM configuration name	Symbol	`routing`	`null`
`fresh_water_density`	ρ_w	×	×
`hydrology_cavitation_opening_coefficient`	c_1		
`hydrology_creep_closure_coefficient`	c_2		
`hydrology_gradient_power_in_flux`	β	×	
`hydrology_hydraulic_conductivity`	k	×	
`hydrology_regularizing_porosity`	ϕ_0		
`hydrology_roughness_scale`	W_r		
`hydrology_thickness_power_in_flux`	α	×	
`hydrology_tillwat_decay_rate`	C_d	×	×
`hydrology_tillwat_max`	W_{til}^{max}	×	×
`ice_density`	ρ_i	×	×
`ice_softness`	A		
`standard_gravity`	g	×	×
`till_c_0`	c_0	×	×
`till_compressibility_coefficient`	C_c	×	×
`till_effective_fraction_overburden`	δ	×	×
`till_reference_effective_pressure`	N_0	×	×
`till_reference_void_ratio`	e_0	×	×

GMDD
7, 4705–4775, 2014

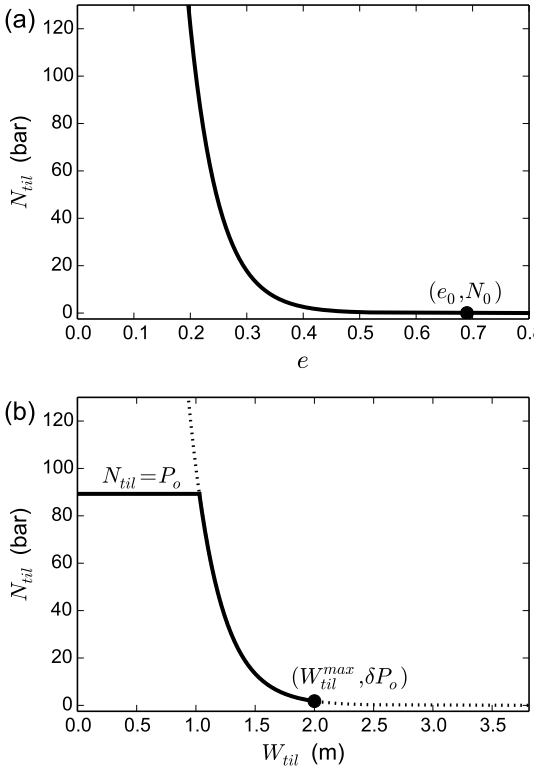

Figure 1. (a) Equation (18) determines the effective pressure N_{til} as a function of the void ratio e, as shown here. Reference values of e_0 and N_0 are indicated. **(b)** The same curve, with N_{til} as a function of W_{til}, and bounded above by overburden pressure P_o and below by a fixed fraction δ of P_o (solid curve), is used in our model. The case shown is for 1000 m ice thickness.

GMDD
7, 4705–4775, 2014

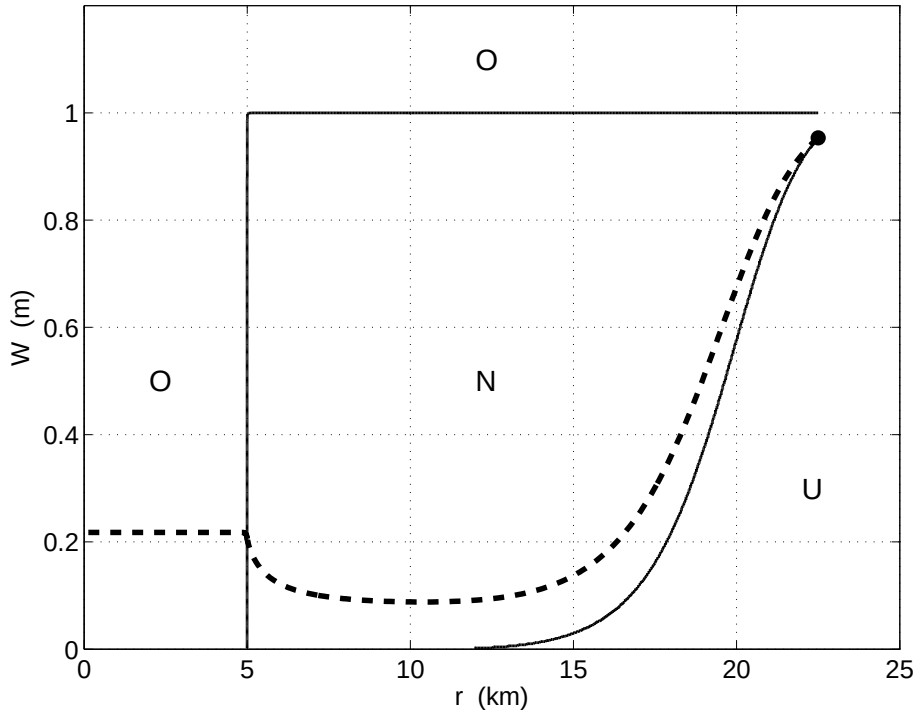

Figure 2. An exact radial, steady solution for water thickness $W(r)$ (dashed). In r-vs.-W space the overpressure (O), normal pressure (N), and underpressure (U) regions are determined by ice geometry and sliding velocity (solid curves; see text).

GMDD
7, 4705–4775, 2014

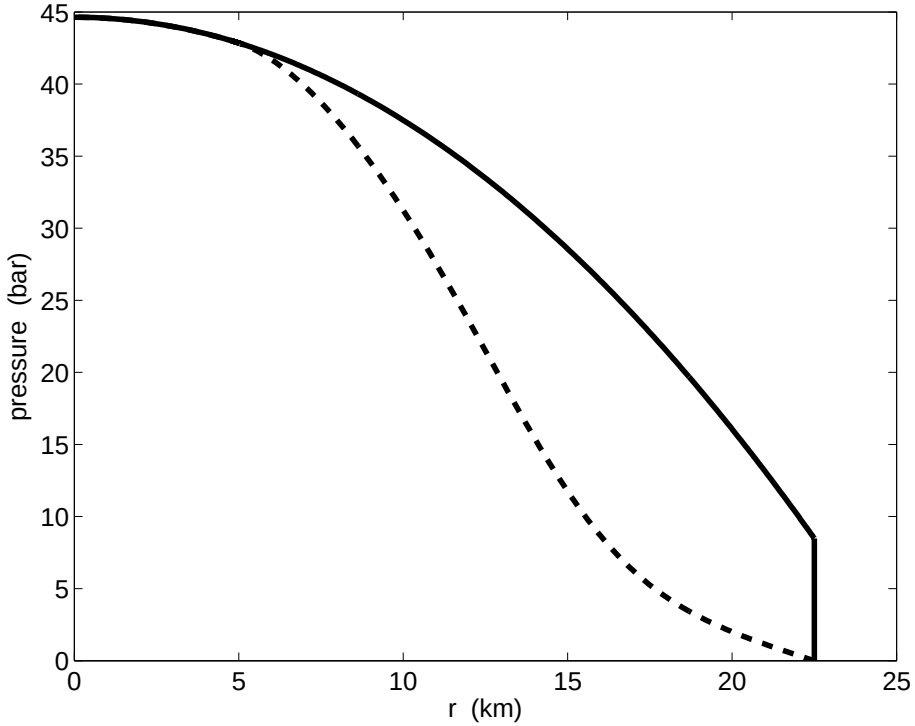

Figure 3. An exact radial, steady solution pressure $P(r)$ (dashed) and overburden pressure P_o (solid).

GMDD
7, 4705–4775, 2014

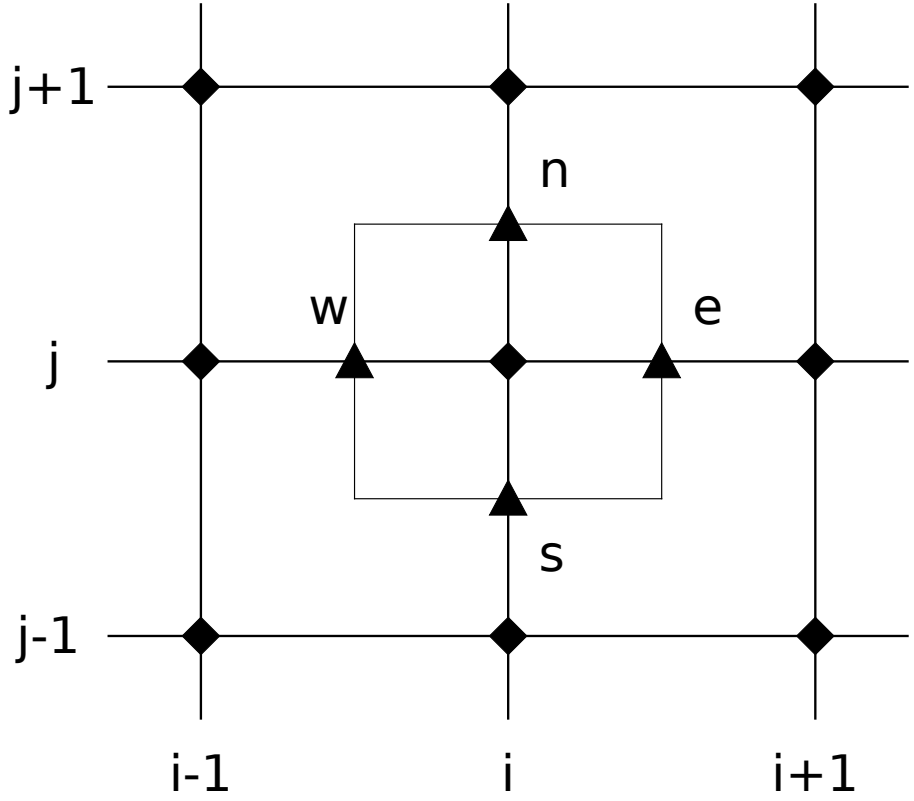

Figure 4. Numerical schemes Eqs. (56) and (64) use a grid-point-centered cell. Velocities, diffusivities, and fluxes are evaluated at staggered grid locations (triangles at centers of cell edges denoted e, w, n, s). State functions W, P are located at regular grid points (diamonds).

GMDD
7, 4705–4775, 2014

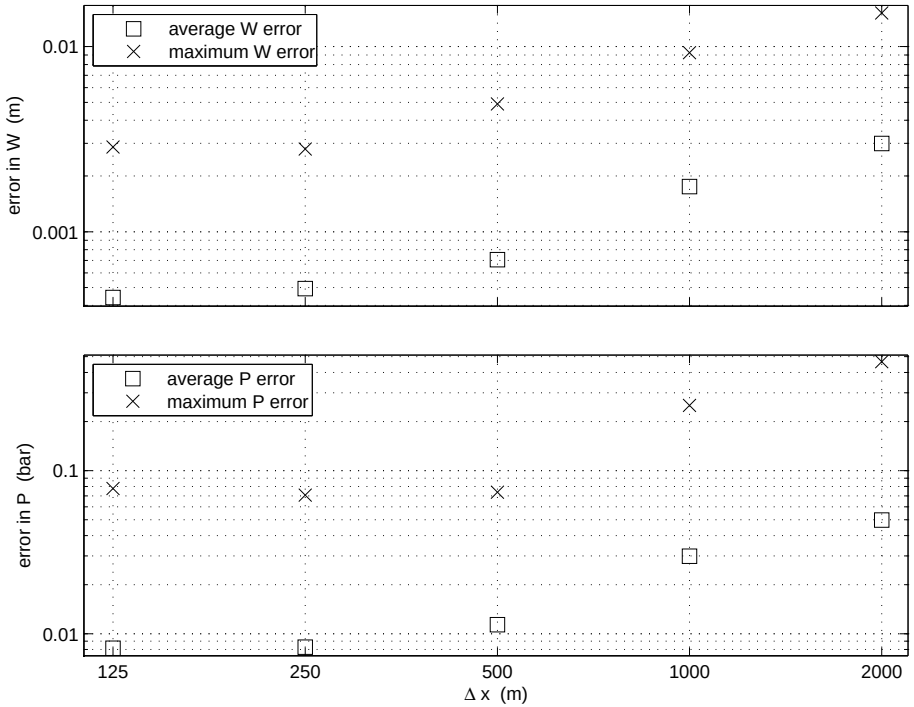

Figure 5. Average water thickness error $|W - W_{\text{exact}}|$ decays as $O(\Delta x^{0.91})$, and average pressure error $|P - P_{\text{exact}}|$ decays as $O(\Delta x^{0.92})$, for grids with spacing $250 \le \Delta x = \Delta y \le 2000$ m.

GMDD
7, 4705–4775, 2014

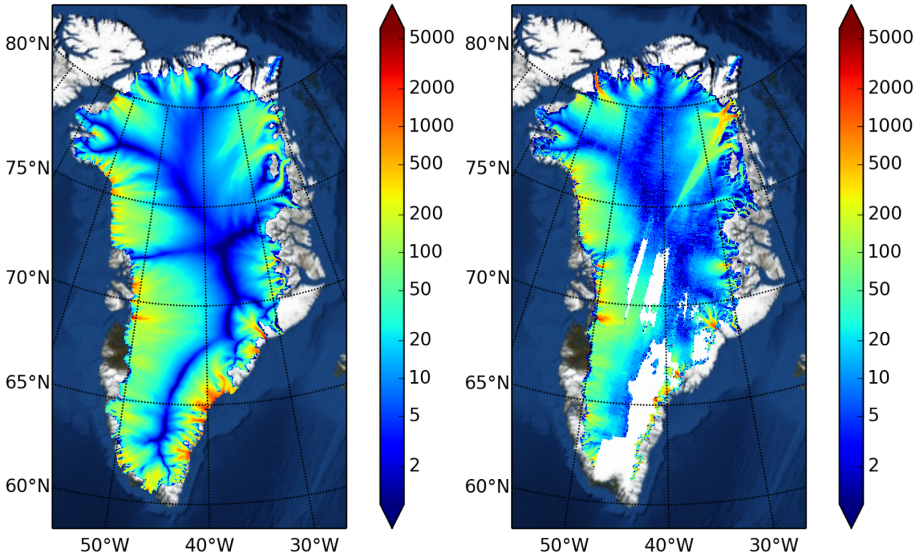

Figure 6. To evaluate the result of the 2 km grid spun-up ice dynamical model we compare modelled ice speed at the ice surface (left; $m a^{-1}$) to satellite observations (right; $m a^{-1}$).

GMDD
7, 4705–4775, 2014

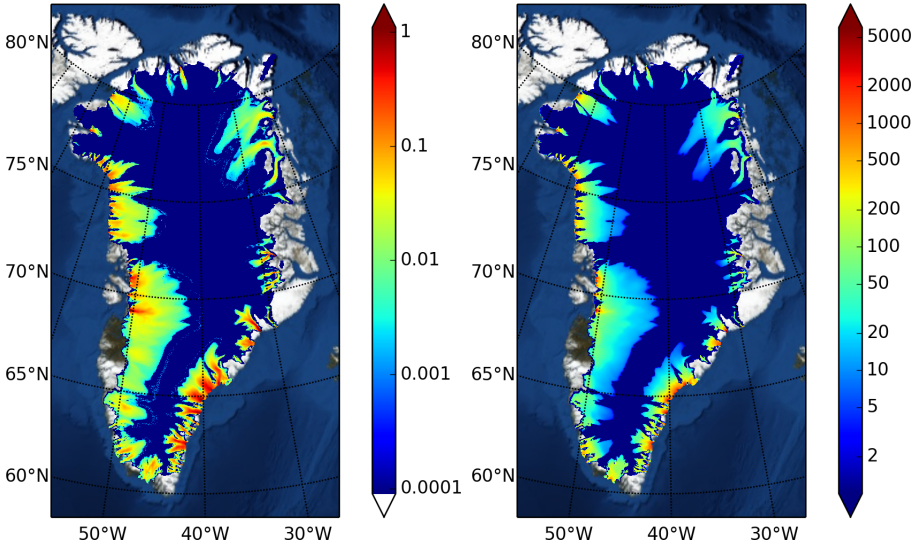

Figure 7. The inputs to the hydrology model are the modeled basal melt rate m/ρ_w (left; m a^{-1}) and sliding speed $|\boldsymbol{v}_b|$ (right; m a^{-1}) from the spun-up model.

GMDD
7, 4705–4775, 2014

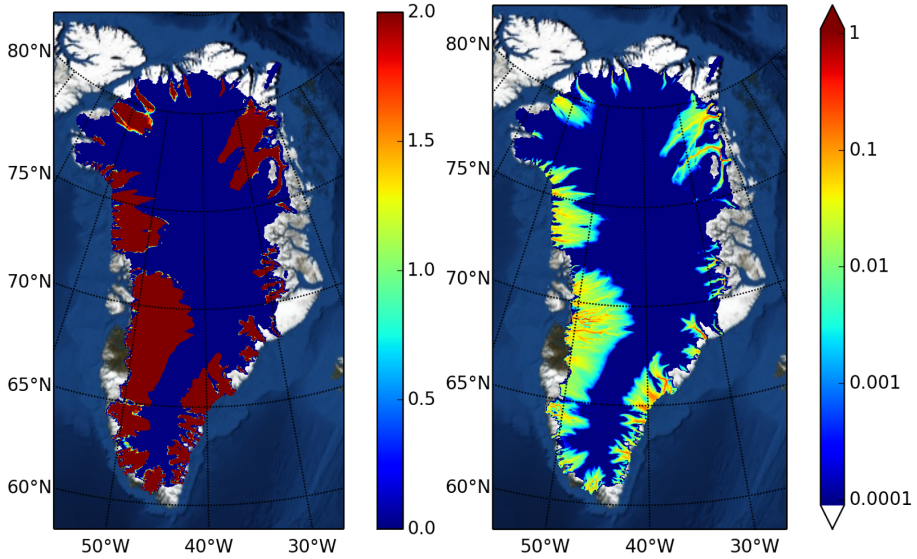

Figure 8. Outputs from the `routing` hydrology model are the modelled till-stored water layer thickness W_{til} (left; m) and modelled transportable water layer thickness W (right; m).

GMDD
7, 4705–4775, 2014

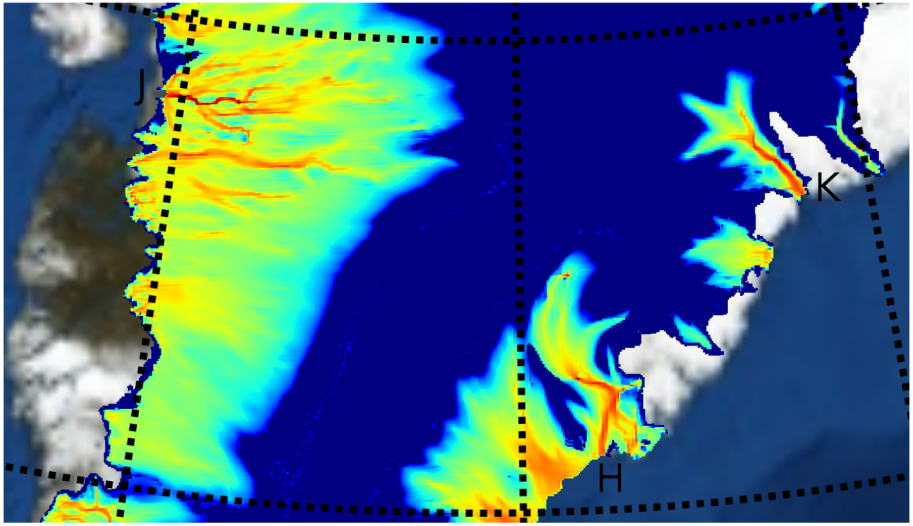

Figure 9. Detail of transportable water *W* plotted in Fig. 8, covering Jakobshavn (J), Helheim (H), and Kangerdlugssuaq (K) outlet glaciers.

GMDD
7, 4705–4775, 2014

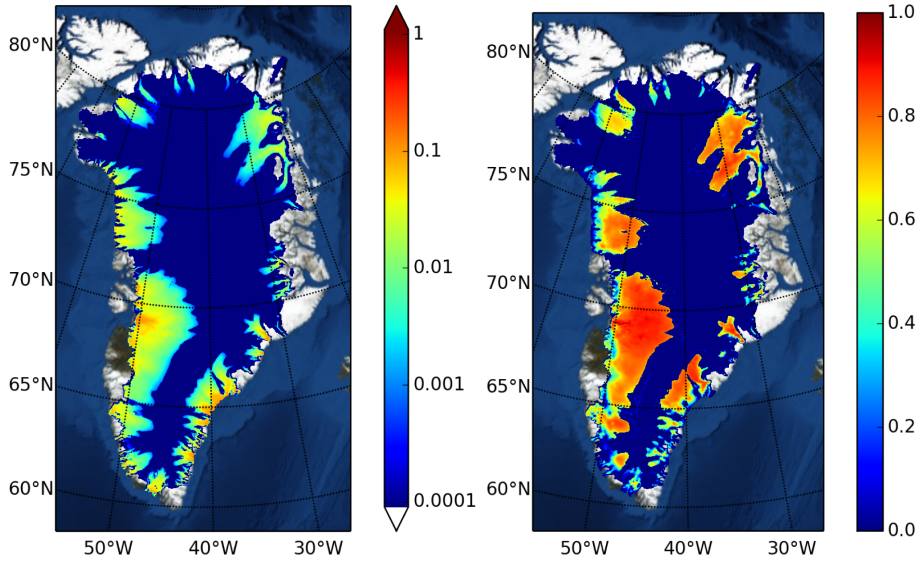

Figure 10. Outputs from the `distributed` hydrology model include the modelled transportable water layer thickness W (left; m), and the modelled transportable water layer pressure, shown relative to overburden pressure P/P_o (right).

GMDD
7, 4705–4775, 2014

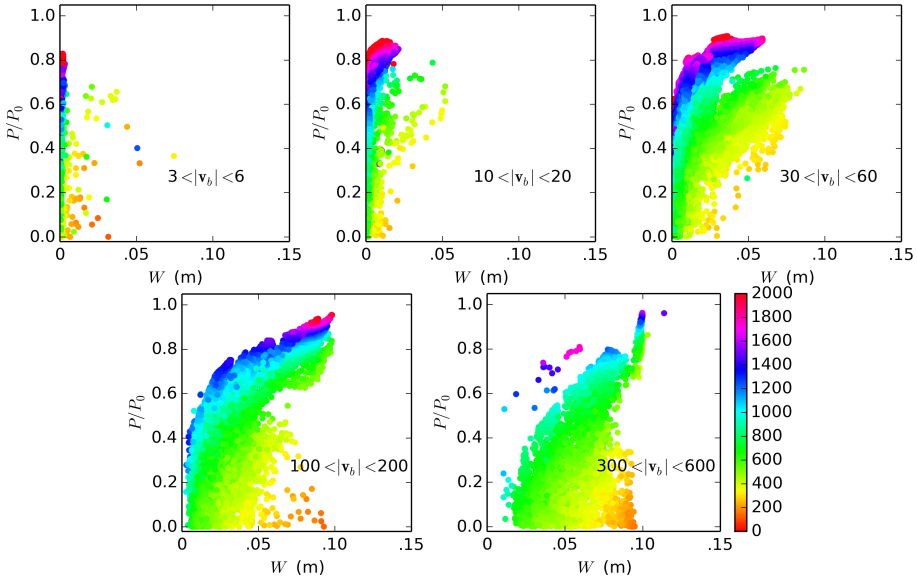

Figure 11. Scatter plots of (W, P) pairs for all cells at end of a 5 model year steady-input simulation on a 2 km grid for the whole Greenland ice sheet using roughness scale $W_r = 0.1$ m. Each scatter plot shows the pairs for a select range of ice sliding speeds, as indicated. Points are colored by ice thickness using a common scale shown beside last figure.

GMDD
7, 4705–4775, 2014

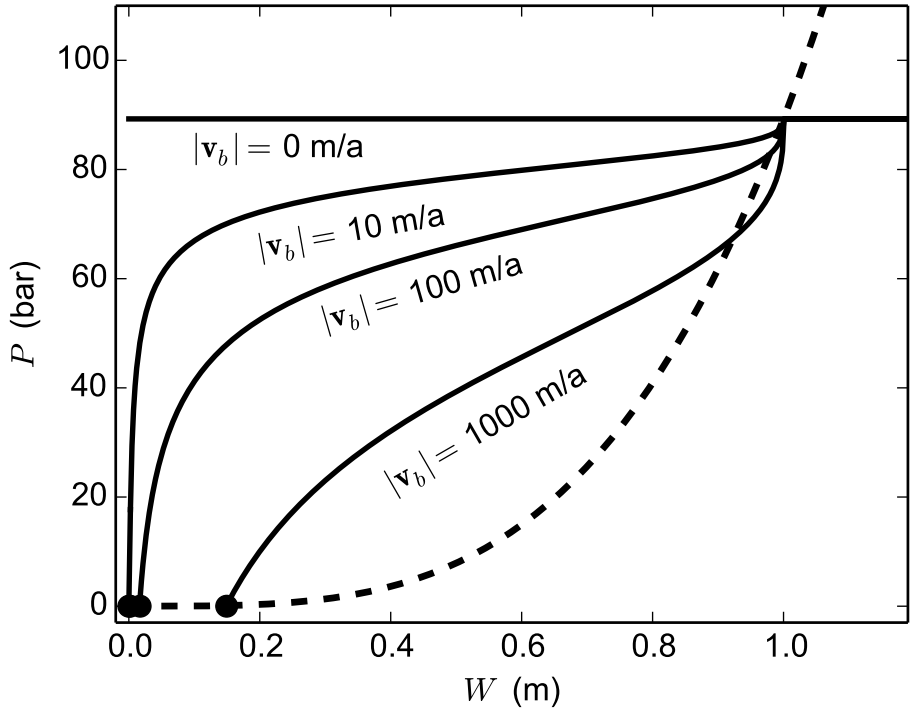

Figure A1. The steady state function $P(W)$ defined by Eq. (A4) depends on the sliding speed $|\boldsymbol{v}_b|$. Four cases are shown. All use W_r = 1 m and a uniform ice thickness of H = 1000 m. Values of W_c are indicated by black dots at P = 0. Relation Eq. (29) (dashed black) is shown with W_{crit} = 1 m for comparison.

GMDD
7, 4705–4775, 2014

Mass-conserving subglacial hydrology in PISM

E. Bueler and W. Van Pelt

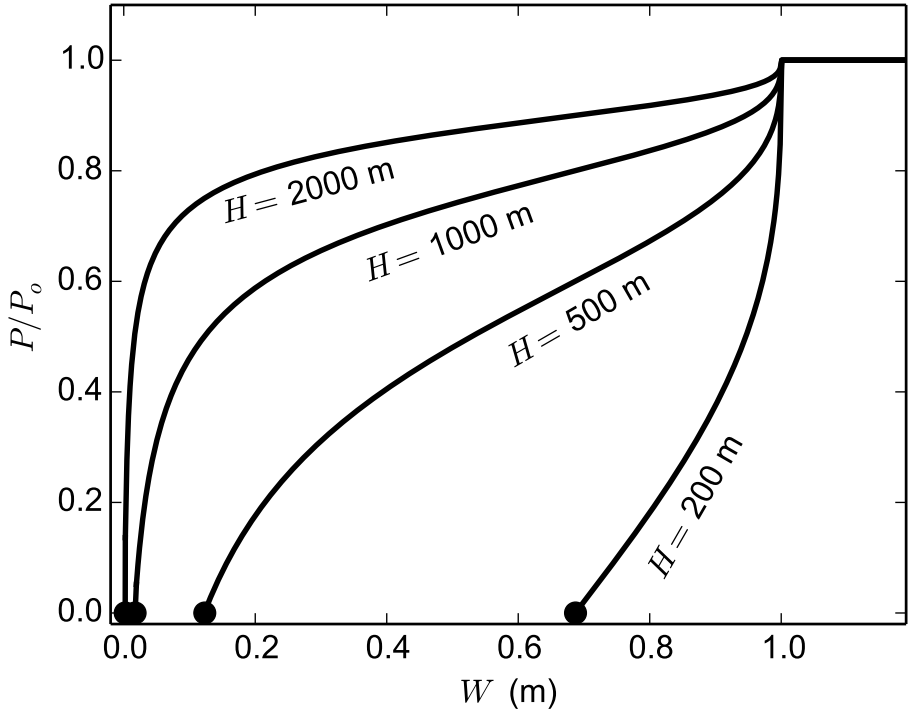

Figure A2. The graph of $P(W)$ defined by Eq. (A4) also depends on overburden pressure $P_o = \rho_i g H$. We fix $|\boldsymbol{v}_b| = 100\,\mathrm{m\,a^{-1}}$ and $W_r = 1\,\mathrm{m}$ and consider four cases of uniform thickness H.

GMDD
7, 4705–4775, 2014